An Internal Variable Theory for Isotropic Visco-elastic-plastic Solids: Application to indentation of amorphous polymeric solids

by

Nicoli Margret Ames

S.B. Mechanical Engineering
Massachusetts Institute of Technology, 2000

Submitted to the Department of Mechanical Engineering
in partial fulfillment of the requirements for the degree of

MASTER OF SCIENCE IN MECHANICAL ENGINEERING

at the

MASSACHUSETTS INSTITUTE OF TECHNOLOGY

June 2003

Author . . . .
Department of Mechanical Engineering
May 9, 2003

Certified by . . . .
Lallit Anand
Professor of Mechanical Engineering
Thesis Supervisor

Accepted by . . . .
Ain A. Sonin
Chairman, Department Committee on Graduate Students

An Internal Variable Theory for Isotropic Visco-elastic-plastic Solids: Application to indentation of amorphous polymeric solids
by
Nicoli Margret Ames

Submitted to the Department of Mechanical Engineering
on May 9, 2003, in partial fulfillment of the
requirements for the degree of
MASTER OF SCIENCE IN MECHANICAL ENGINEERING

Abstract

A significant advance in modeling the plastic deformation of amorphous polymers has been made by Parks, Argon, Boyce, Arruda, and their co-workers (e.g. Parks, Argon, & Bagepalli, 1985; Boyce, Parks, & Argon, 1998; Arruda & Boyce, 1993), and by Wu and Van der Giessen (1993). Although these models phenomenologically capture the *large deformation elastic-viscoplastic* response of these materials in a reasonably accurate manner, they do not adequately account for the *creep* response of these materials at stress levels below those causing "macro-yield", as well as the Bauschinger-type reverse yielding phenomena at strain levels less than $\approx 30\%$ associated with the macro-yield transient. Anand (2003) has recently generalized the model of Anand and Gurtin (2003) to begin to capture these important aspects of these material's mechanical response. In this work, we summarize Anand's three-dimensional theory and then specialize the constitutive equations to an approximate one-dimensional form. Also, we describe our monotonic, cyclic and creep experiments on the amorphous polymeric solid poly(methyl methacrylate) (PMMA), at ambient temperature and stress states under which this material does not exhibit crazing, and we outline detailed procedures for material parameter determination from these experiments. We have implemented the three-dimensional constitutive equations in the finite-element computer program ABAQUS/Explicit (ABAQUS, Inc., 2002), and using this finite-element program, we show numerical results to some representative problems in microindentation, and compare them against corresponding results from physical experiments.

Thesis Supervisor: Lallit Anand
Title: Professor of Mechanical Engineering

Acknowledgments

Contents

4

List of Figures

Chapter 1

Introduction

A significant advance in modeling the plastic deformation of amorphous polymers has been made by Parks, Argon, Boyce, Arruda, and their co-workers (e.g. Parks et al., 1985; Boyce et al., 1998; Arruda & Boyce, 1993), and by Wu and Van der Giessen (1993). Recently, Anand and Gurtin (2003) have generalized the work of these authors and developed a *frame-indifferent and thermodynamically consistent* theory for the plasticity of amorphous polymers under isothermal conditions below their *glass transition temperatures*. Although these models phenomenologically capture the *large deformation elastic-viscoplastic* response of these materials in a reasonably accurate manner, they do not adequately account for the *creep* response of these materials at stress levels below those causing "macro-yield", as well as the Bauschinger-type reverse yielding phenomena at strain levels less than $\approx 30\%$ associated with the macro-yield transient. A reasonable model for the "small-strain" ($\lesssim 30\%$) viscoelastic response is of importance to describe the structural response of components made from these materials.

Anand (2003) has recently generalized the model of Anand and Gurtin (2003) to begin to capture important aspects of the complex mechanical response associated with the macro-yield transient of these materials. Anand's theory is based on the mathematical approach and physical ideas contained in the paper by Anand and Gurtin (2003) and, following these authors, he also utilizes the Kröner-Lee decomposition, $\mathbf{F} = \mathbf{F}^e \mathbf{F}^p$, of the deformation gradient $\mathbf{F}$ into elastic and plastic parts, $\mathbf{F}^e$ and $\mathbf{F}^p$ (Kroner, 1960; Lee, 1969), and also assumes that the plastic flow is irrotational $\mathbf{W}^p = \mathbf{0}$, so that the evolution equa-

tion for $\mathbf{F}^p$ is $\dot{\mathbf{F}}^p = \mathbf{D}^p\mathbf{F}^p$, with $\mathbf{D}^p$ deviatoric. However, as a departure from the previous theory he assumes further that $\mathbf{D}^p$ is given by the sum of $N+1$ micro-mechanisms, such that $\mathbf{D}^p = \sum_{\alpha=0}^{N} \mathbf{D}^{p\,(\alpha)}$. He chooses the inelastic micro-mechanism indexed by $\alpha = 0$ to represent the dominant "macro-yield" response, while the inelastic micro-mechanisms indexed by $\alpha = 1, \ldots, N$ are chosen to represent the finer details of the "viscoelastic" response of the material associated with the macro-yield transient. Correspondingly, he introduces $\boldsymbol{\xi} = (s^{(0)}, s^{(1)}, s^{(2)}, \ldots, s^{(N)})$, a list of (N+1) positive-valued scalar fields, and another list of (N+1) symmetric tensor fields $\boldsymbol{\mathcal{A}} = (\mathbf{A}^{(0)}, \mathbf{A}^{(1)}, \mathbf{A}^{(2)}, \ldots, \mathbf{A}^{(N)})$, that represent aspects of the intermolecular resistances to plastic flow associated with each inelastic micro-mechanism. Further, since a key feature controlling the macro-yield of amorphous materials is known to be the evolution of the local free-volume associated with the metastable state of these materials, he also utilizes a scalar internal variable φ that represents the local free-volume. Introduction of these internal-state variables allows the model to phenomenologically capture important aspects of the creep response of solid polymers prior to macro-yield, as well as the highly non-linear stress-strain behavior that precedes the yield-peak and gives rise to post-yield strain-softening. Anand's theory explicitly accounts for the dependence of the Helmholtz free energy on the tensorial internal state variables in a thermodynamically consistent manner. This dependence leads directly to backstresses in the underlying flow rule, and allows the model to capture aspects of the strong Bauschinger-type reverse-yielding phenomena typically observed in amorphous polymeric solids upon unloading after inelastic deformations.

The plan of this thesis is as follows. We summarize Anand's (2003) three-dimensional theory in Chapter 2. In Chapter 3 we specialize the constitutive equations to an approximate one-dimensional form. In Chapter 4 we describe our monotonic, cyclic and creep experiments on the amorphous polymeric solid poly(methyl methacrylate) (PMMA), at ambient temperature and stress states under which this material does not exhibit crazing. In Chapter 5 we outline detailed procedures for material parameter determination from appropriate experiments. We have implemented the three-dimensional constitutive equations in the finite-element computer program ABAQUS/Explicit (ABAQUS, Inc., 2002). Using this finite-element program, in Chapter 6 we show numerical results to some representa-

tive problems in microindentation, and compare them against corresponding results from physical experiments.

Chapter 2

Three-Dimensional Constitutive Equations for Amorphous Polymers

In this section we summarize Anand's (2003) constitutive model for large elastic-viscoplastic deformations of amorphous polymeric materials under isothermal conditions at temperatures below their glass transition temperature. The underlying constitutive equations relate the following basic fields:

ψ,		free energy density per unit volume of the relaxed configuration,
$\mathbf{T}$,	$\mathbf{T} = \mathbf{T}^\top$,	Cauchy stress,
$\mathbf{F}$,	$J = \det \mathbf{F} > 0$,	deformation gradient,
$\mathbf{F}^p$,	$\det \mathbf{F}^p = 1$	plastic deformation gradient,
$\mathbf{F}^e = \mathbf{F}\mathbf{F}^{p-1}$,	$\det \mathbf{F}^e > 0$,	elastic part of the deformation gradient,
$\mathbf{F}^e = \mathbf{R}^e \mathbf{U}^e$		polar decomposition of $\mathbf{F}^e$,
$\mathbf{U}^e = \sum_{\alpha=1}^{3} \lambda_\alpha^e \, \mathbf{r}_\alpha \otimes \mathbf{r}_\alpha$		spectral decomposition of $\mathbf{U}^e$,
$\mathbf{E}^e = \sum_{\alpha=1}^{3} E_\alpha^e \, \mathbf{r}_\alpha \otimes \mathbf{r}_\alpha$,	$E_\alpha^e = \ln \lambda_\alpha^e$,	logarithmic elastic strain,

$$\mathbf{F}^* = J^{-1/3}\mathbf{F}, \qquad \text{distortional part of } \mathbf{F},$$

$$\mathbf{C}^* = \mathbf{F}^{*\top}\mathbf{F}^*, \qquad \text{right Cauchy-green tensor correspond-}$$

ing to $\mathbf{F}^*$,

$$\mathbf{B}^* = \mathbf{F}^*\mathbf{F}^{*\top}, \qquad \text{left Cauchy-green tensor corresponding}$$

to $\mathbf{F}^*$,

$$\mathcal{A} = (\mathbf{A}^{(0)}, \dots, \mathbf{A}^{(N)}), \quad \mathbf{A}^{(\alpha)} = \mathbf{A}^{(\alpha)\top}, \quad \text{tensorial internal variables,}$$

$$\boldsymbol{\xi} = (s^{(0)}, \dots, s^{(N)}), \qquad s^{(\alpha)} > 0 \qquad \text{scalar internal variables,}$$

$$\varphi \qquad \text{internal variable representing free vol-}$$

ume.

The special set of constitutive equations is summarized below:

1. **Free Energy**:

$$\psi = \psi^e(\mathbf{E}^e) + \Psi(\mathbf{C}^*) + \sum_{\alpha=0}^{N} \xi^\alpha(\mathbf{A}^{(\alpha)}, \varphi). \tag{2.1}$$

Here,

$$\psi^e = G|\mathbf{E}_0^e|^2 + \tfrac{1}{2}K|\mathrm{tr}\,\mathbf{E}^e|^2, \tag{2.2}$$

where $G > 0$ and $K > 0$ are the elastic shear and bulk moduli, respectively.

For $\Psi(\mathbf{C}^*)$ we define a *effective (distortional) stretch*

$$\bar{\lambda} \stackrel{\text{def}}{=} \tfrac{1}{\sqrt{3}}\sqrt{\mathrm{tr}\,\mathbf{C}^*}, \tag{2.3}$$

and adopt the *Langevin-inverse* form

$$\Psi = \mu_R\,\lambda_L^2\left[\left(\frac{\bar{\lambda}}{\lambda_L}\right)x + \ln\left(\frac{x}{\sinh x}\right) - \left(\frac{1}{\lambda_L}\right)y - \ln\left(\frac{y}{\sinh y}\right)\right], \tag{2.4}$$

$$x = \mathcal{L}^{-1}\left(\frac{\bar{\lambda}}{\lambda_L}\right), \qquad y = \mathcal{L}^{-1}\left(\frac{1}{\lambda_L}\right), \tag{2.5}$$

where $\mathcal{L}^{-1}$ is the inverse of the Langevin function $\mathcal{L}(\dots) = \coth(\dots) - (\dots)^{-1}$. The material parameter μ_R is called the *rubbery modulus*, and λ_L is called the *network locking stretch*.

For the free energies $\xi^\alpha(\mathbf{A}^{(\alpha)}, \varphi)$ we define *effective stretches*

$$\lambda^{(\alpha)} \overset{\text{def}}{=} \frac{1}{\sqrt{3}} \sqrt{\operatorname{tr} \mathbf{A}^{(\alpha)}}, \tag{2.6}$$

and adopt the simple *neo-Hookean* form

$$\xi^\alpha = \mu^{(\alpha)} \frac{3}{2} \left\{ \left(\lambda^{(\alpha)}\right)^2 - 1 \right\}, \qquad \mu^{(\alpha)} = \hat{\mu}^{(\alpha)}(\varphi), \quad \alpha = 0, \dots, N; \tag{2.7}$$

the material parameters $\mu^{(\alpha)}$ are called *back stress moduli*.

2. **Equation for the stress**:

$$\left. \begin{aligned} \mathbf{T} &= \mathbf{T}_A + \mathbf{T}_B, \qquad \text{with} \\ \mathbf{T}_A &= J^{-1} \mathbf{R}^e \left(\mathbf{S}_A^e\right) \mathbf{R}^{e\top}, \qquad \mathbf{S}_A^e = 2G\mathbf{E}_0^e + K(\operatorname{tr}\mathbf{E}^e)\mathbf{1}, \\ \mathbf{T}_B &= J^{-1} \mu_B \mathbf{B}_0^*, \qquad \mu_B = \mu_R \left(\frac{\lambda_L}{3\bar{\lambda}}\right) \mathcal{L}^{-1}\left(\frac{\bar{\lambda}}{\lambda_L}\right). \end{aligned} \right\} \tag{2.8}$$

3. **Equation for the backstresses**:

$$\mathbf{S}_{\text{back}}^{(\alpha)} = \mu^{(\alpha)} \mathbf{A}^{(\alpha)}, \qquad \alpha = 0, \dots, N. \tag{2.9}$$

4. **Flow rule**: The evolution equation for $\mathbf{F}^p$ is

$$\dot{\mathbf{F}}^p = \mathbf{D}^p \mathbf{F}^p, \qquad \mathbf{F}^p(\mathbf{X}, 0) = \mathbf{1}, \tag{2.10}$$

with $\mathbf{D}^p$ given by the sum of plastic stretchings from $(N+1)$ micro-mechanisms

$$\mathbf{D}^p = \sum_{\alpha=0}^{N} \nu^{(\alpha)} \left(\frac{(\mathbf{S}_A^e)_0 - (\mathbf{S}_{\text{back}}^{(\alpha)})_0}{2\bar{\tau}^{(\alpha)}} \right), \qquad \nu^{(\alpha)} = \nu_0 \left(\frac{\bar{\tau}^{(\alpha)}}{s^{(\alpha)} + \alpha_p^{(\alpha)}\pi} \right)^{\frac{1}{m^{(\alpha)}}}, \tag{2.11}$$

where

$$\bar{\tau}^{(\alpha)} = \frac{1}{\sqrt{2}} |(\mathbf{S}_A^e)_0 - (\mathbf{S}_{\text{back}}^{(\alpha)})_0|, \tag{2.12}$$

is an *equivalent shear stress* for each micro-mechanism, and

$$\pi = -\frac{1}{3}\operatorname{tr}\mathbf{S}_A^e, \tag{2.13}$$

is a mean normal pressure. The quantity $\nu^{(\alpha)}$ is an *equivalent plastic shear strain rate* for the αth micro-mechanism, and is taken in a simple power law form, with ν_0 a *reference plastic shear strain rate*, and $0 < m^{(\alpha)} \leq 1$ are *strain rate sensitivity parameters*. The limit $m^{(\alpha)} \to 0$ corresponds to the rate-independent limit, while $m^{(\alpha)} = 1$ corresponds to the linearly viscous limit. Also, $\alpha_p^{(\alpha)}$ are *pressure sensitivity* parameters for each micro-mechanism.

5. The evolution equation for the internal variables $\mathbf{A}^{(\alpha)}$ are taken as

$$\dot{\mathbf{A}}^{(\alpha)} = \mathbf{D}^{p(\alpha)}\mathbf{A}^{(\alpha)} + \mathbf{A}^{(\alpha)}\mathbf{D}^{p(\alpha)}, \quad \mathbf{A}^{(\alpha)}(\mathbf{X},0) = \mathbf{1}. \tag{2.14}$$

6. We consider the evolution equations for $s^{(0)}$ and φ in the special coupled rate independent form

$$\left.\begin{aligned}\dot{s}^{(0)} &= h_0\left(1 - \frac{s^{(0)}}{\tilde{s}^{(0)}(\varphi)}\right)\nu^{(0)}, \\ \dot{\varphi} &= g_0\left(\frac{s^{(0)}}{s_{\mathrm{cv}}^{(0)}} - 1\right)\nu^{(0)},\end{aligned}\right\} \tag{2.15}$$

with

$$\tilde{s}^{(0)}(\varphi) = s_{\mathrm{cv}}^{(0)}[1 + b(\varphi_{\mathrm{cv}} - \varphi)], \tag{2.16}$$

where $\{h_0, g_0, s_{\mathrm{cv}}^{(0)}, b, \varphi_{\mathrm{cv}}\}$ are additional material parameters. The initial values of $s^{(0)}$ and φ are denoted by

$$s_i^{(0)} \quad \text{and} \quad \varphi_i.$$

The remaining scalar internal variables $s^{(\alpha)}$ are assumed to be constants:

$$s^{(\alpha)} = s_i^{(\alpha)}, \qquad \alpha = 1, \dots, N. \tag{2.17}$$

where $s_i^{(\alpha)}$ denote their initial values.

7. Finally, the backstress moduli $\mu^{(\alpha)}$ are taken to evolve with the free-volume φ according to

$$\dot{\mu}^{(\alpha)} = c^{(\alpha)}\left(1 - \frac{\mu^{(\alpha)}}{\mu_{\text{sat}}^{(\alpha)}}\right)\dot{\varphi}, \qquad \mu^{(\alpha)}(\phi_i) = \mu_i^{(\alpha)} \tag{2.18}$$

where $\mu_i^{(\alpha)}$ are the initial values of $\mu^{(\alpha)}$ when φ is equal to its initial value φ_i, while $c^{(\alpha)} > 0$, and $\mu_{\text{sat}}^{(\alpha)} > 0$ are material constants for each α. We expect that $\mu_{\text{sat}}^{(\alpha)} \leq \mu_i^{(\alpha)}$, so that $\mu^{(\alpha)}$ decreases to its final value $\mu_{\text{sat}}^{(\alpha)}$ as φ increases.

To complete the constitutive model for a particular amorphous polymeric material the constitutive parameter/functions that need to be specified are

$$\left\{G, K, \mu_R, \lambda_L, \nu_0, m^{(\alpha)}, \alpha_p^{(\alpha)}, h_0, g_0, s_{\text{cv}}^{(0)}, b, \varphi_{\text{cv}}, s_i^{(0)}, \varphi_i, s_i^{(\alpha)}, \mu_i^{(\alpha)}, c^{(\alpha)}, \mu_{\text{sat}}^{(\alpha)}\right\}.$$

Chapter 3

One-Dimensional Constitutive Equations for Amorphous Polymers

In order to expedite the material parameter calibration process, we have developed an approximate one-dimensional version of the constitutive model that we will implement in MATLAB and use to determine the material parameters from the experiments to be described in the next chapter. The one-dimensional model is outlined in the first section of this chapter. All phenomena, except compressibility and pressure sensitivity of the material, are represented in the one-dimensional model. We have chosen to use an explicit integration procedure for the differential equations, and the MATLAB code is shown in Appendix A. A discussion of the one-dimensional model, including an equivalent rheological model, is also presented.

The underlying constitutive equations relate the following basic fields:

ψ, free energy density,

per unit volume of the relaxed configuration,

σ, Cauchy stress,

$U > 0$, stretch,

U^p, plastic stretch,

$U^e = UU^{p-1}$, elastic part of the stretch,

$\epsilon = \ln U$, logarithmic strain,

$\epsilon^e = \ln U^e$, logarithmic elastic strain,

$\mathcal{A} = (A^{(0)}, \ldots, A^{(N)})$, stretch-like internal variables,

$\xi = (s^{(0)}, \ldots, s^{(N)})$, $\quad s^{(\alpha)} > 0$, scalar internal variables,

φ, internal variable representing free volume.

The special set of one-dimensional constitutive equations is summarized below:

1. **Free Energy**:

$$\psi = \psi^e(\epsilon^e) + \Psi(U) + \sum_{\alpha=0}^{N} \xi^\alpha(A^{(\alpha)}, \varphi). \tag{3.1}$$

Here,

$$\psi^e = \tfrac{1}{2} E |\epsilon^e|^2, \tag{3.2}$$

where $E > 0$ is the Young's modulus.

For $\Psi(U)$ we define an *effective stretch*[1]

$$\bar{\lambda} \equiv \tfrac{1}{\sqrt{3}}\sqrt{U^2 + 2U^{-1}}, \tag{3.3}$$

and adopt the *Langevin-inverse* form

$$\Psi = \mu_R \, \lambda_L^2 \left[\left(\frac{\bar{\lambda}}{\lambda_L}\right) x + \ln\left(\frac{x}{\sinh x}\right) - \left(\frac{1}{\lambda_L}\right) y - \ln\left(\frac{y}{\sinh y}\right)\right], \tag{3.4}$$

$$x = \mathcal{L}^{-1}\left(\frac{\bar{\lambda}}{\lambda_L}\right), \qquad y = \mathcal{L}^{-1}\left(\frac{1}{\lambda_L}\right), \tag{3.5}$$

where $\mathcal{L}^{-1}$ is the inverse of the Langevin function $\mathcal{L}(\ldots) = \coth(\ldots) - (\ldots)^{-1}$. The material parameter μ_R is called the *rubbery modulus*, and λ_L is called the *network locking stretch*.

For the free energies $\xi^\alpha(A^{(\alpha)}, \varphi)$ we define *effective stretches*

$$\lambda^{(\alpha)} \equiv \tfrac{1}{\sqrt{3}}\sqrt{\left(A^{(\alpha)}\right)^2 + 2\left(A^{(\alpha)}\right)^{-1}}, \tag{3.6}$$

and adopt the simple *neo-Hookean* form

$$\xi^\alpha = \mu^{(\alpha)} \frac{3}{2}\left\{\left(\lambda^{(\alpha)}\right)^2 - 1\right\}, \qquad \mu^{(\alpha)} = \hat{\mu}^{(\alpha)}(\varphi), \quad \alpha = 0, \ldots, N; \tag{3.7}$$

where $\mu^{(\alpha)}$ are called *back stress moduli*.

---

[1]Let (A_1, A_2, A_3) denote the set of a principal stretches of a symmetric positive definite tensor $\mathbf{A}$ in three dimensions representing a stretch tensor. For incompressibility of such a stretch, the A_i satisfy

$$A_1 A_2 A_3 = 1.$$

The *effective value* $\bar{A}$ of the stretch is defined by

$$\bar{A} \stackrel{\text{def}}{=} \frac{1}{\sqrt{3}}\sqrt{A_1^2 + A_2^2 + A_3^2}.$$

In one-dimension, with $A \stackrel{\text{def}}{=} A_1$, $A_2 = A_3 = A^{-\frac{1}{2}}$, the effective value is

$$\bar{A} = \frac{1}{\sqrt{3}}\sqrt{A^2 + 2\,A^{-1}}.$$

2. **Equation for the stress**: [2]

$$\left.\begin{aligned}
\sigma &= \sigma_A + \sigma_B \\
\sigma_A &= E\epsilon^e \\
\sigma_B &= \mu_B \left(U^2 - U^{-1}\right), \qquad \mu_B = \mu_R \left(\frac{\lambda_L}{3\bar{\lambda}}\right) \mathcal{L}^{-1}\left(\frac{\bar{\lambda}}{\lambda_L}\right)
\end{aligned}\right\} \tag{3.8}$$

3. **Equation for the backstresses**:

$$\sigma^{(\alpha)}_{\text{back}} = \mu^{(\alpha)} \left[\left(A^{(\alpha)}\right)^2 - \left(A^{(\alpha)}\right)^{-1}\right], \qquad \alpha = 0, \dots, N. \tag{3.9}$$

4. **Flow rule**: The evolution equation for U^p is

$$\dot{U}^p = D^p U^p, \qquad U^p(0) = 1, \tag{3.10}$$

with D^p given by the sum of plastic stretchings from $(N+1)$ micro-mechanisms

$$D^p = \sum_{\alpha=0}^{N} D^{p(\alpha)} = \sum_{\alpha=0}^{N} \dot{\epsilon}^{p(\alpha)} \operatorname{sign}(\sigma_A - \sigma^{(\alpha)}_{\text{back}}), \tag{3.11}$$

$$\dot{\epsilon}^{p(\alpha)} = \dot{\epsilon}_0 \left(\frac{|\sigma_A - \sigma^{(\alpha)}_{\text{back}}|}{s^{(\alpha)}}\right)^{\frac{1}{m^{(\alpha)}}}, \tag{3.12}$$

---

[2]Given a free energy function of the form

$$\psi = \hat{\psi}\left(\bar{\lambda}\right), \qquad \bar{\lambda} = \frac{1}{\sqrt{3}}\sqrt{\lambda^2 + 2\lambda^{-1}},$$

the engineering stress S is defined by

$$S = \frac{\partial \psi}{\partial \lambda} = \frac{\partial \hat{\psi}}{\partial \bar{\lambda}} \frac{\partial \bar{\lambda}}{\partial \lambda}.$$

Also, assuming incompressibility

$$A_0 = A\lambda,$$

where A_0 is the original cross-sectional area and A is the current cross-sectional area. The Cauchy stress σ can then be represented as

$$\sigma = S\lambda = \lambda \frac{\partial \hat{\psi}}{\partial \bar{\lambda}} \frac{\partial \bar{\lambda}}{\partial \lambda},$$

and for a simple neo-Hookean free energy this gives

$$\sigma = \mu \left(\lambda^2 - \lambda^{-1}\right).$$

The quantity $\dot{\epsilon}^{p(\alpha)}$ is a *plastic strain rate* for the α-th micro-mechanism, and is taken in a simple power law form, with $\dot{\epsilon}_0$ a *reference plastic strain rate*, and $0 < m^{(\alpha)} \leq 1$ are *strain rate sensitivity parameters*. The limit $m^{(\alpha)} \to 0$ corresponds to the rate-independent limit, while $m^{(\alpha)} = 1$ corresponds to the linearly viscous limit.

5. The evolution equation for the internal variables $A^{(\alpha)}$ are taken as

$$\dot{A}^{(\alpha)} = D^{p(\alpha)} A^{(\alpha)}, \qquad A^{(\alpha)}(0) = 1. \tag{3.13}$$

6. We consider the evolution equations for $s^{(0)}$ and φ in the special coupled rate-independent form

$$\left.\begin{aligned}
\dot{s}^{(0)} &= h_0 \left(1 - \frac{s^{(0)}}{\tilde{s}^{(0)}(\varphi)} \right) \dot{\epsilon}^{p(0)}, \\
\dot{\varphi} &= g_0 \left(\frac{s^{(0)}}{s_{\mathrm{cv}}^{(0)}} - 1 \right) \dot{\epsilon}^{p(0)}
\end{aligned}\right\} \tag{3.14}$$

with

$$\tilde{s}^{(0)}(\varphi) = s_{\mathrm{cv}}^{(0)}[1 + b(\varphi_{\mathrm{cv}} - \varphi)], \tag{3.15}$$

where $\left\{ h_0, g_0, s_{\mathrm{cv}}^{(0)}, b, \varphi_{\mathrm{cv}}, \right\}$ are additional material parameters. The initial values of $s^{(0)}$ and φ are denoted by

$$s_i^{(0)}, \qquad \text{and} \qquad \varphi_i. \tag{3.16}$$

The remaining scalar internal variables $s^{(\alpha)}$ are assumed to be constants:

$$s^{(\alpha)} = s_i^{(\alpha)}, \qquad \alpha = 1, \ldots, N. \tag{3.17}$$

where $s_i^{(\alpha)}$ denote their initial values.

7. Finally the backstress moduli $\mu^{(\alpha)}$ are taken to evolve with the free-volume φ according to

$$\dot{\mu}^{(\alpha)} = c^{(\alpha)} \left(1 - \frac{\mu^{(\alpha)}}{\mu_{\mathrm{sat}}^{(\alpha)}} \right) \dot{\varphi}, \qquad \mu^{(\alpha)}(\varphi_i) = \mu_i^{(\alpha)} \tag{3.18}$$

where $\mu_i^{(\alpha)}$ is the initial value of $\mu^{(\alpha)}$ when φ is equal to its initial value φ_i, while $c^{(\alpha)} > 0$, and $\mu_{\text{sat}}^{(\alpha)} > 0$ are material constants for each α. We expect that $\mu_{\text{sat}}^{(\alpha)} \leq \mu_i^{(\alpha)}$, so that $\mu^{(\alpha)}$ decreases to its final value $\mu_{\text{sat}}^{(\alpha)}$ as φ increases.

To complete the one-dimensional constitutive model for a particular amorphous polymeric material the constitutive parameters/functions that need to be specified are

$$\left\{ E, \mu_R, \lambda_L, \dot{\epsilon}_0, m^{(\alpha)}, h_0, g_0, s_{\text{cv}}^{(0)}, b, \varphi_{\text{cv}}, \varphi_i, s_i^{(\alpha)}, \mu_i^{(\alpha)}, c^{(\alpha)}, \mu_{\text{sat}}^{(\alpha)} \right\}$$

This one-dimensional constitutive model can be visualized using a simple rheological representation as shown in Figure 3-1. The rheological model consists of two arms, Ⓐ and Ⓑ, in parallel. In system Ⓐ there are $N + 1$ spring-dashpot *micro-mechanisms* that are arranged in series together with a spring element. This arm accounts for small-strain behavior, which we will define as strains below approximately 30%. For each spring-dashpot micro-mechanism we have chosen a neo-Hookean type model for the springs where the stiffness of each spring is $\mu^{(\alpha)}$. The dashpots follow a standard power-law type flow rule where the strain rate in each dashpot is $\dot{\epsilon}^{p(\alpha)}$ and the internal resistance of each dashpot is $s^{(\alpha)}$. Viscoelastic effects are controlled by the $\alpha = 1, \ldots, N$ micro-mechanisms. The stiffness of each of these springs, $\mu^{(\alpha)}$, is allowed to evolve and soften, while the internal resistance of each of the dashpots, $s^{(\alpha)}$, is held constant. The $\alpha = 0$ micro-mechanism is responsible for the behavior around the yield peak, which will be referred to as the viscoplastic macro-yield behavior. The spring stiffness of this system, $\mu^{(0)}$, is held constant, however, the internal resistance of the dashpot, $s^{(0)}$, evolves with the free volume. System Ⓑ consists of a non-linear Langevin-type spring and gives rise to chain-locking at large stretches.
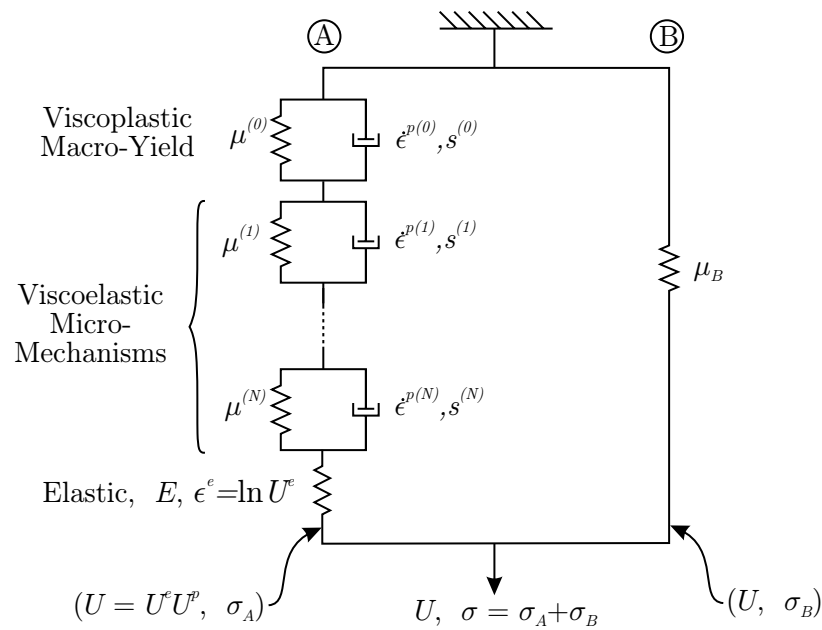
Figure 3-1: One-dimensional rheological representation of the proposed model with multiple stretch-like internal variables, each representing an α-th micro-mechanism.

Chapter 4

Experiments

This chapter covers the experiments that were conducted on poly(methyl methacrylate) (PMMA), which is the material we have chosen to calibrate and verify the proposed model.

4.1   Experimental Procedures

The material used in these experiments was purchased from a commercial vendor in the form of 1 inch diameter cast rods. All specimens were annealed after machining by heating in a furnace to the glass transition temperature, 105 C, and holding at that temperature for two hours. The specimens were then allowed to slowly cool in the furnace to room temperature over a period of several hours. All tests were performed at room temperature under isothermal conditions.

All compression and tension experiments were conducted using a biaxial servo-hydraulic Instron testing machine having a normal load capacity of 220 kN over an axial travel of 100 mm and a torque capacity of 2.2 kN-m over a rotational travel of 95°. All strains were measured using an extensometer with a 12.7 mm gauge section and ±6.35 mm travel. Data acquisition was performed on a desktop PC. LabView 6, a customizable data acquisition software package, interfaces with the Instron through a National Instruments PCI card installed in the PC. Raw data was sampled at 1 kHz, however, Labview performed real time averaging before recording data, resulting in a smoothed output with an artificial sampling rate of 4 Hz.

Because PMMA crazes in tension and is known to undergo deformation by shear-yielding in compression, compression is the optimum mode of deformation to extract properties for our model which does not account for crazing. Two testing procedures were employed, simple compression and compression-tension; they are outlined in the following sections. All tests, except for creep, were carried out using displacement control, with rates ranging from 0.01 mm/s to 0.1 mm/s. Figure 4-1 shows a plot of strain versus time of a test conducted at 0.01 mm/s. As can be seen, for strains below about 50%, displacement control can be a reasonable approximation of strain control.
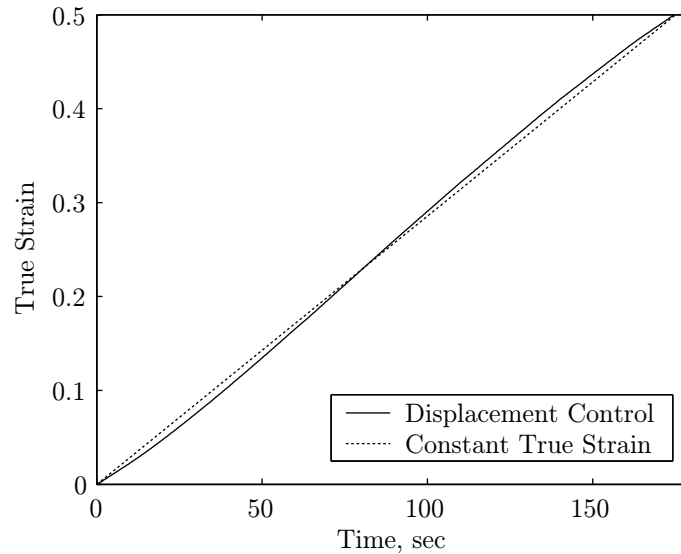
Figure 4-1: Comparison of displacement and strain control for true strains less than 50%.

4.1.1   Uniaxial Compression

Ensuring homogeneous deformation throughout the specimen is critical for a uniaxial compression test, however, the inherent friction between the testing machine's compression plattens and the specimen often results in inhomogeneous deformation where the mid-section of the specimen has a much larger diameter change than the sections in contact with the plattens. This phenomenon is referred to as "barrelling". To reduce the friction, the steel plattens were polished to a mirror finish using a 1 micrometer Alumina slurry, and 0.010" thick Teflon films were placed between the specimen and the plattens. Oils and greases are

not recommended as lubricants because they may attack or dissolve PMMA specimens, or cause them to craze.

In order to eliminate the effects of the testing machine's compliance in compression, an extensometer was used to measure strain. A fairly large specimen was required to accommodate the extensometer; this specimen is shown in Figure 4-2. Care was taken to ensure that the loads required to deform this large-diameter specimen were obtainable by the testing machine.
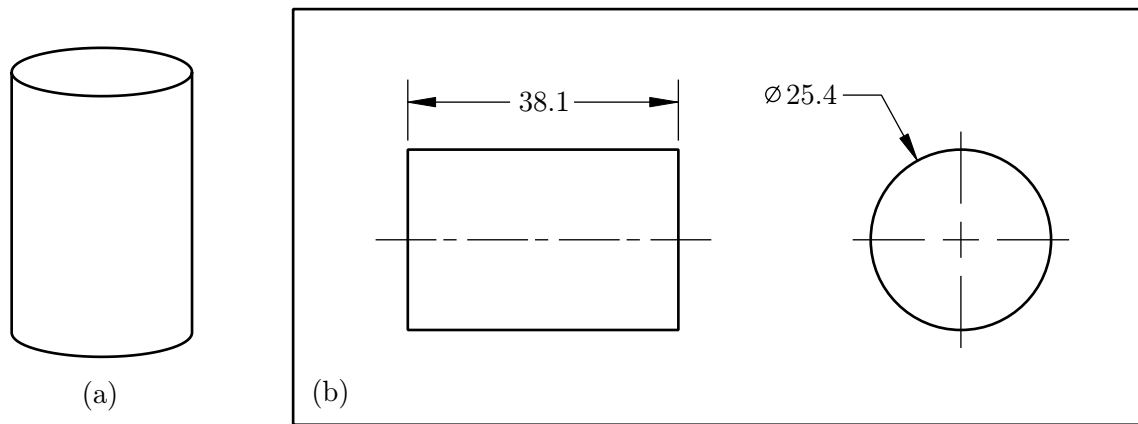

(a)   (b)

Figure 4-2: Specimen used for uniaxial compression experiments. All dimensions are in millimeters. (a) Isometric view of specimen. (b) Engineering drawing.

4.1.2   Compression-Tension

In order to get a complete observation of the non-linear unloading response of PMMA, the specimen needed to be pulled slightly into tension after a compression load/unload cycle. Also, it is desirable to do small-strain cyclic loading. These types of loading conditions may be accomplished by using a "stubby" tension specimen as shown in Figure 4-3; this will be referred to as a compression-tension specimen. Here the gauge length is relatively close in size to the diameter in order to minimize the chance of buckling while in compression. Obtaining a homogeneous state of deformation is impossible with such a specimen, however, barrelling was minimal at strains below approximately 20%. Beyond this point the material exhibits appreciable strain softening and it becomes very difficult to prevent barrelling with the boundary conditions imposed by this specimen.
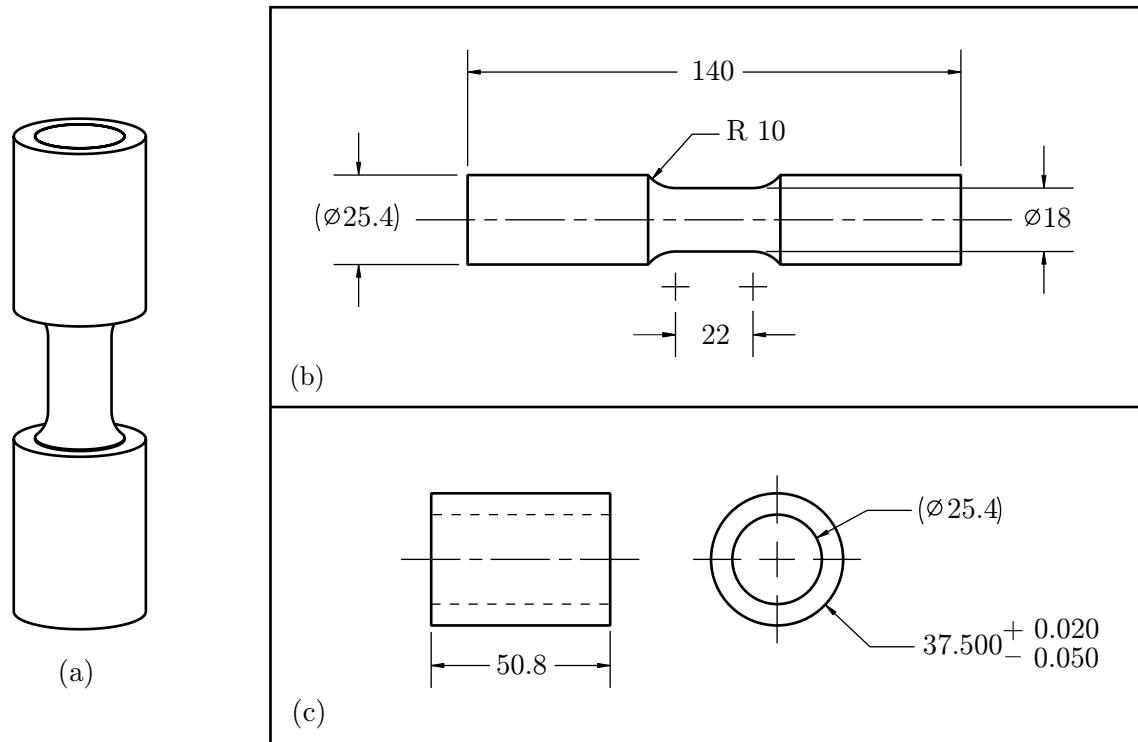
Figure 4-3: Specimen used for compression-tension experiments. All dimensions are in millimeters. (a) Isometric view of assembled specimen. (b) PMMA specimen engineering drawing. (c) Aluminum sleeve engineering drawing.

Once again, this specimen is oversized as compared to standard specimens in order to accommodate the placement of an extensometer on the gauge section. Also, experience showed that gripping the PMMA directly would cause it to fracture in the grips due to the uneven inner surface of the grips. Thus, aluminum sleeves were designed to slip tightly over the gripping section of the specimen, see Figure 4-3c. The aluminum deformed easily in the grips and transmitted a very homogeneous pressure to the PMMA specimen in order to hold it firmly without fracture occurring. In addition, because of the high loads required to deform this large specimen, there was a very high risk that the specimen would slip either in the testing machine's grips or at the aluminum/PMMA interface, thus a relatively high gripping pressure of 4500 psi was used.

4.2 Experimental Results

4.2.1 Loading - Unloading

The typical stress-strain response of PMMA undergoing compressive loading and subsequent unloading is illustrated in Figure 4-4. This data is reproduced from Hasan (1994). Each curve represents a separate specimen, and all tests were conducted at a relatively low strain-rate of -0.001 s^{-1}. Initially, the response is nearly linear, but as the strains rise beyond about 4%, the material begins to soften. The local maximum stress at approximately 9% strain is commonly referred to as the yield point. Beyond this point, the softening continues until a minimum is reached at approximately 30%. After this, the stress once again rises as the polymer chains begin to align and lock. The unloading curvature is also shown to increase as the maximum loading strain is increased.

4.2.2 Rate Sensitivity

The experiments shown in Figure 4-5 exemplify the rate sensitivity of PMMA. All tests were conducted using simple compression specimens, and each curve represents a fresh specimen. The yield stress of PMMA is shown to increase by approximately 10% when increasing the strain rate from -0.0003 s^{-1} to -0.003 s^{-1}. Notice that for these rates and strains, the unloading curvature seems to be fairly constant.

4.2.3 Strain Recovery

After each of the experiments in Figure 4-5 was conducted, the amount of strain recovered at zero load was recorded for approximately 10 minutes. The recovered strain versus time for the tests with maximum strains between 13% and 50% and conducted at a strain rate of -0.0003 s^{-1} is shown in Figure 4-6. The amount of recovered strain is fairly consistent for each strain level. Figure 4-7 shows the recovered strain for two specimens that were compressed to a maximum strain of 20% at strain rates of -0.0003 s^{-1} to -0.003 s^{-1}. The specimen compressed at higher strain rate exhibits much faster strain recovery.

4.2.4 Compression-Tension

Results for compression-tension tests at moderate and low strains are shown in Figure 4-8 and Figure 4-9 respectively. The left-most curve in Figure 4-8 is identical to the right-most curve in Figure 4-9. Post-yield (beyond 9% strain), the unloading curve smoothly transitions into a soft linear region once the tension regime is reached. However, for the specimens that were unloaded prior to yield, the unloading curve also softens considerably, yet it becomes slightly stiffer as the tension regime is reached.

4.2.5 Cyclic Loading

Low-strain cyclic compression-tests symmetric about zero strain are shown in Figure 4-10. Each sub-figure represents a separate specimen cycled at strains of $\pm 1\%$, $\pm 2\%$, $\pm 3\%$, and $\pm 4\%$. All tests were commenced in compression. Arrows on the figures indicate the direction of movement of the loops as the number of cycles increases. Beyond the $\pm 1\%$ test, it can be seen that the first cycle is slightly stiffer than the remaining cycles. Also, even at strains as small as $\pm 1\%$, there is clear evidence of hysteresis in the stress-strain response. Yet, once each of these specimens was allowed to relax at room temperature, they each completely recovered any residual strains within a few minutes. This evidence highlights the viscoelastic properties of PMMA. Furthermore, the specimen that was cycled at $\pm 4\%$ strain was again cycled at $\pm 4\%$ strain three days later. Figure 4-11 shows the results of the two tests which are clearly identical, which indicates that no inelastic deformation may have occurred in the specimen. However, the second test ended when the specimen failed due to crazing just prior to the peak of the tension regime of the third cycle. This is evidence that crazes in PMMA can develop during cyclic loading, even with what seems to be a relatively low strain condition.

Due to PMMA's susceptibility to crazing in tension, further cyclic loading tests at higher strains were carried out while remaining completely in the compressive strain regime. These results are shown in Figure 4-12. Each sub-figure represents a fresh specimen, and as before, arrows on the figures indicate the direction of movement of the loops as the number of cycles increase. As in the low-strain cyclic experiments, the first cycle is much stiffer than the

following cycles. Also, only the first cycle travels through the yield peak, while the remaining cycles follow a much simpler and symmetrical path.

4.2.6   Creep

Creep tests were carried out at pre-yield stress levels of 24 MPa, 50 MPa, 63 MPa, and 75 MPa. The input stress for each test is shown in Figure 4-13. The strain-time results are show in Figure 4-14. The amount of creep strain for each test (measured as the amount of strain after the stress has been applied) are approximately 0.15%, 0.7%, 1.6%, and 3%.

An ideal creep test would be conducted by applying a true stress step at time zero, but this is a difficult condition to obtain in the laboratory. Yet, for relatively small creep strains and long hold times, we can approximate this condition by ramping up to a specified force over a period of a few seconds and then holding that force constant for the required creep time (in our tests this is one hour, or 3600 seconds). The true stress levels that correspond to the strain-time profiles in Figure 4-14 are shown in Figure 4-13. It is clear that our experimental conditions are a very good approximation of an ideal creep test. When the stress levels become closer to the yield stress of the material, however, the creep strains become quite large and it is no longer possible to approximate a constant true stress state with a constant force state.
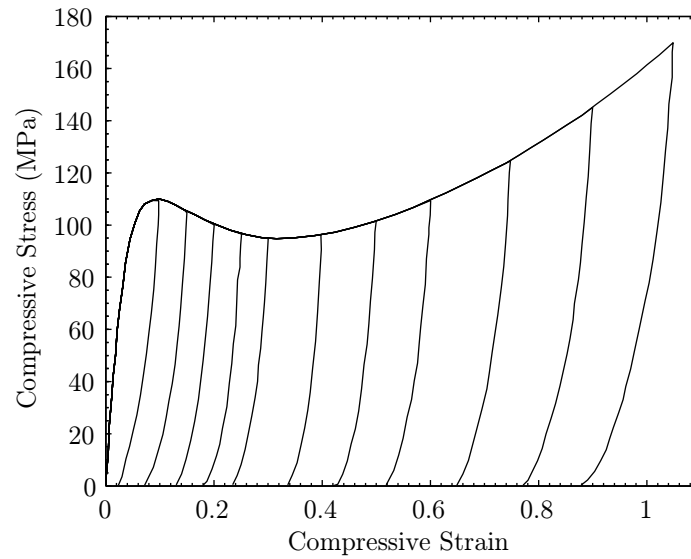
Figure 4-4: Simple compression tests on annealed PMMA at 296 K and a constant true strain rate of -0.001 s^{-1}. Each curve represents a separate specimen. (Hasan, 1994)
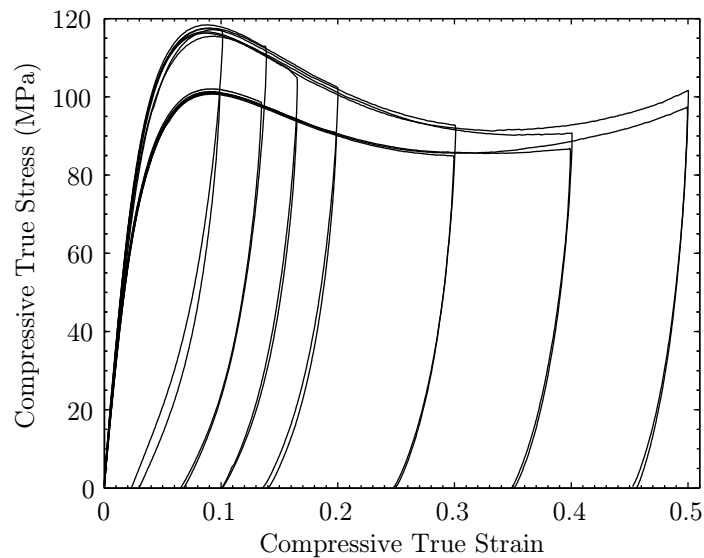

Figure 4-5: Simple compression tests on annealed PMMA at room temperature and two different strain rates. The top set of curves represents a strain rate of -0.003 s^{-1}, and the bottom set represents a strain rate of -0.0003 s^{-1}. Each curve represents a separate specimen.
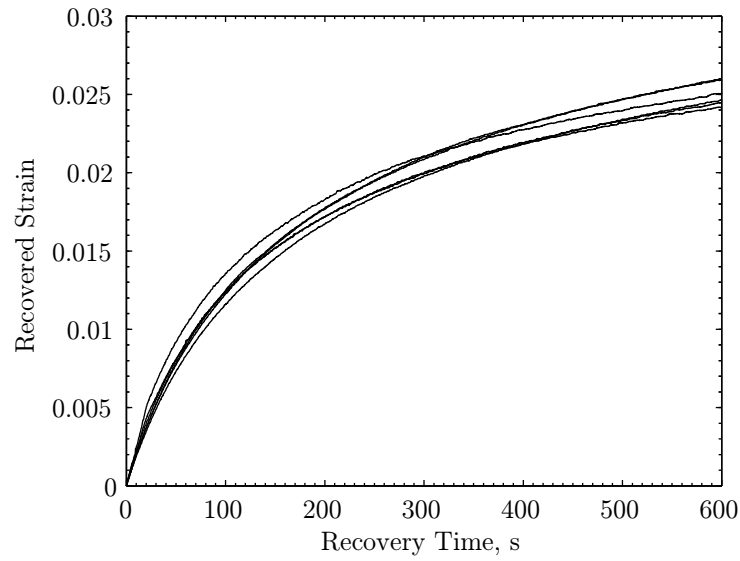
Figure 4-6: Recovery strain for simple compression tests on annealed PMMA at room temperature to a maximum strains between 13% and 50%. Each curve represents a separate specimen.
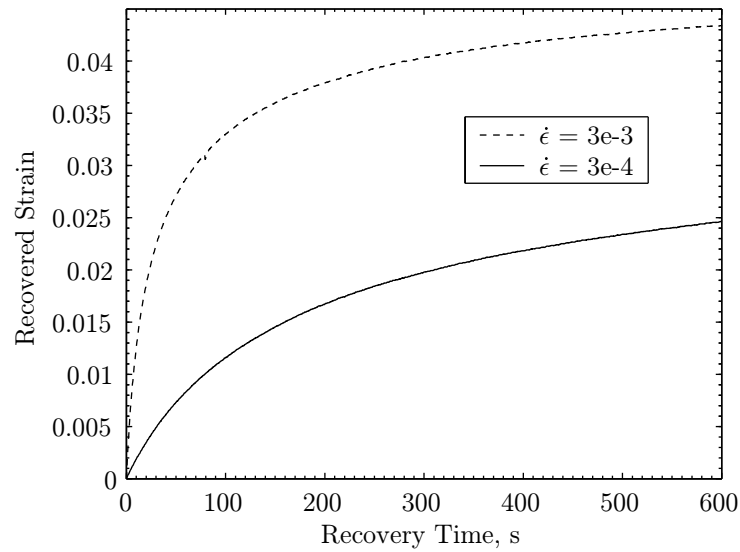
Figure 4-7: Recovery strain for simple compression tests on annealed PMMA at room temperature and two different strain rates to a maximum strain of approximately 20%. Each curve represents a separate specimen.
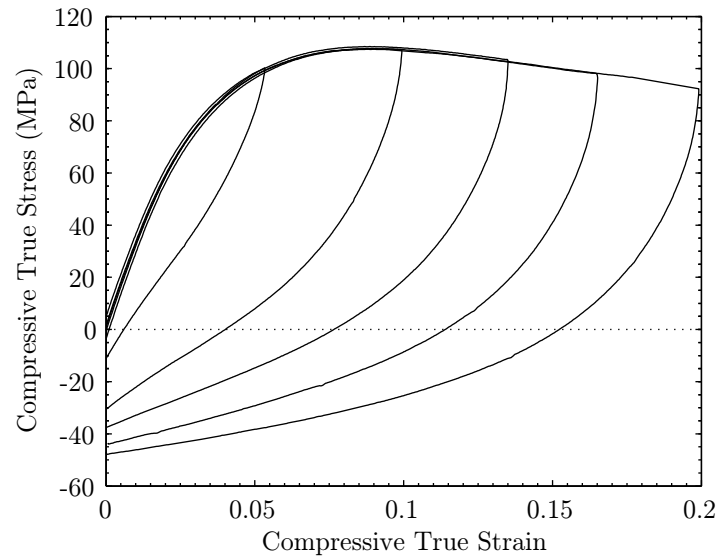
Figure 4-8: Compression-tension tests on annealed PMMA at room temperature at a strain rate of $-0.0003 \ \mathrm{s}^{-1}$. Each curve represents a separate specimen.
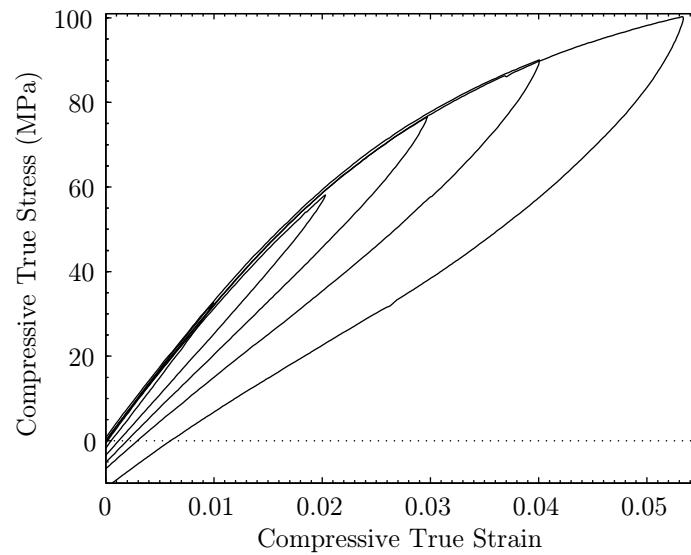
Figure 4-9: Low-strain compression-tension tests on annealed PMMA at room temperature at a strain rate of $-0.0003 \ \mathrm{s}^{-1}$. Each curve represents a separate specimen. The right-most curve is identical to the left-most curve in Figure 4-8

Figure 4-10: Low-strain cyclic compression-tension tests on annealed PMMA at room temperature at a strain rate of -0.0003 s^{-1}. Arrows indicate the direction of movement of the loops as the number of cycles increase. (a) $\pm 1\%$ true strain (b) $\pm 2\%$ true strain (c) $\pm 3\%$ true strain (d) $\pm 4\%$ true strain.
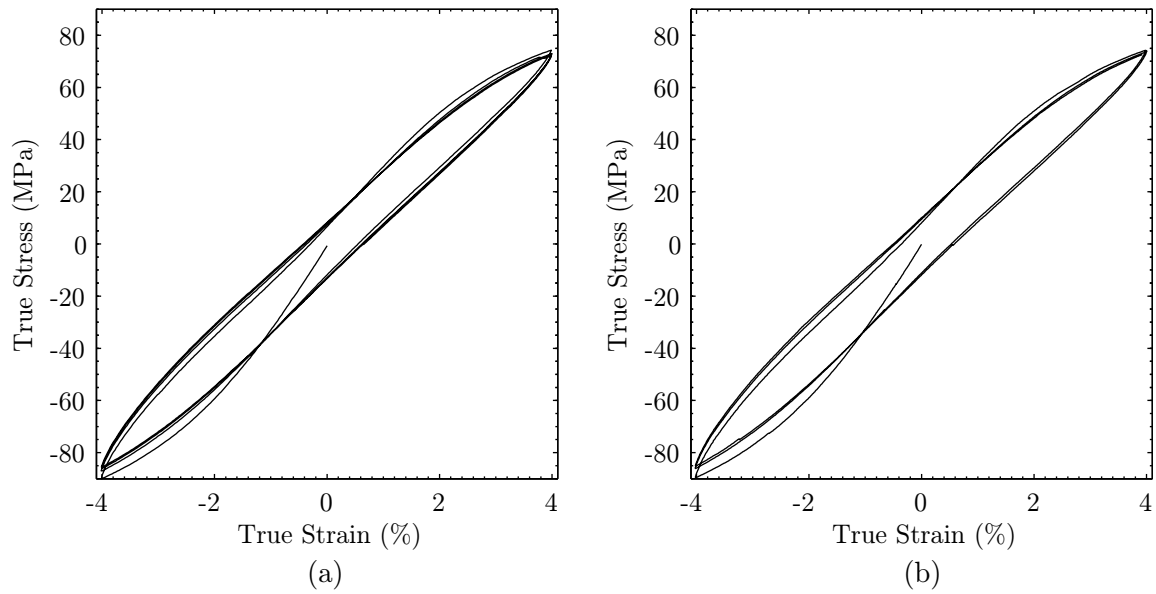
Figure 4-11: Repeated ±4% strain cyclic compression-tension tests on the same specimen of annealed PMMA at room temperature at a strain rate of -0.0003 s^{-1}. (a) First test. (b) Second test on same specimen three days later. Specimen failed due to crazing at peak of tension portion of third cycle.
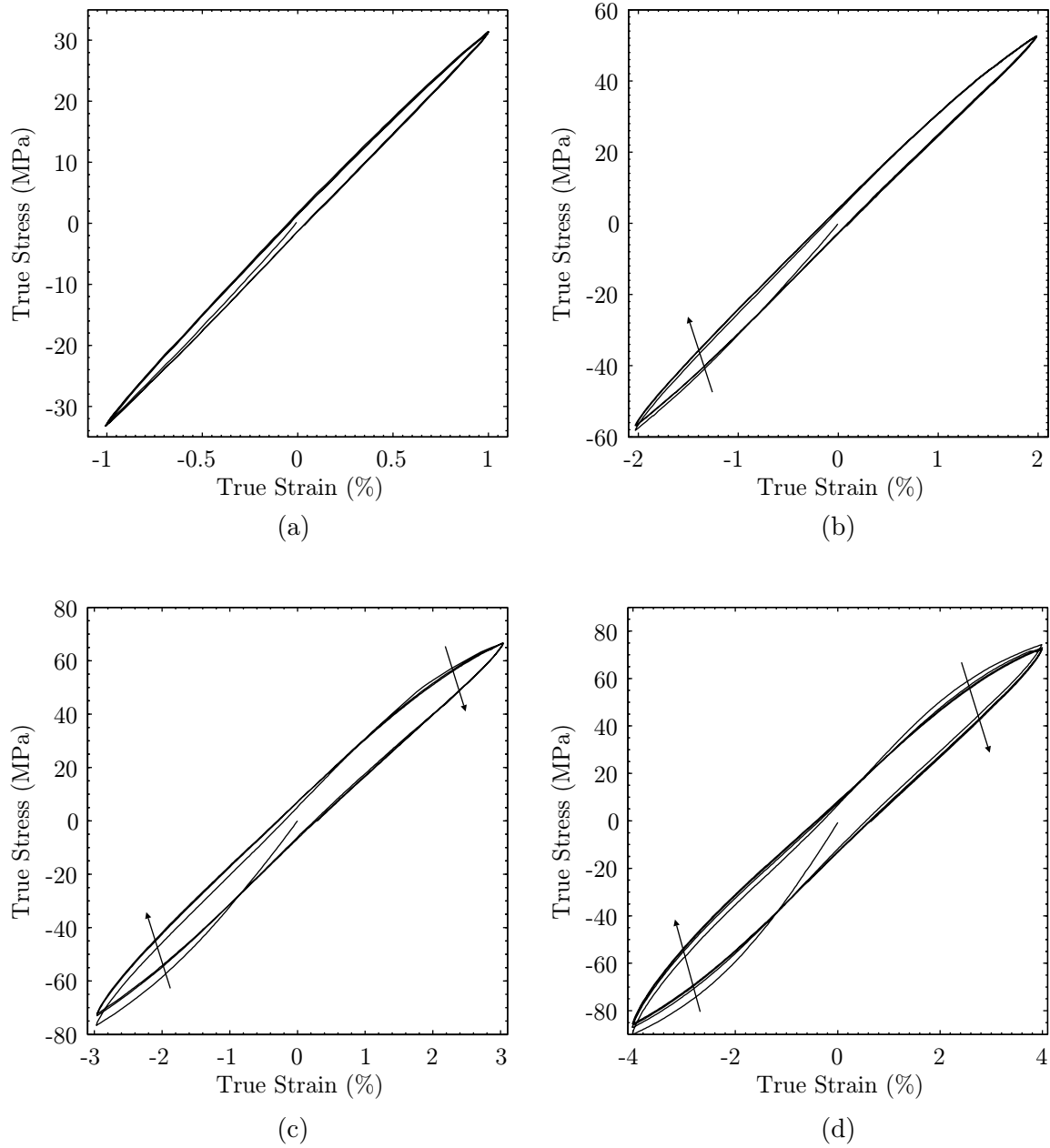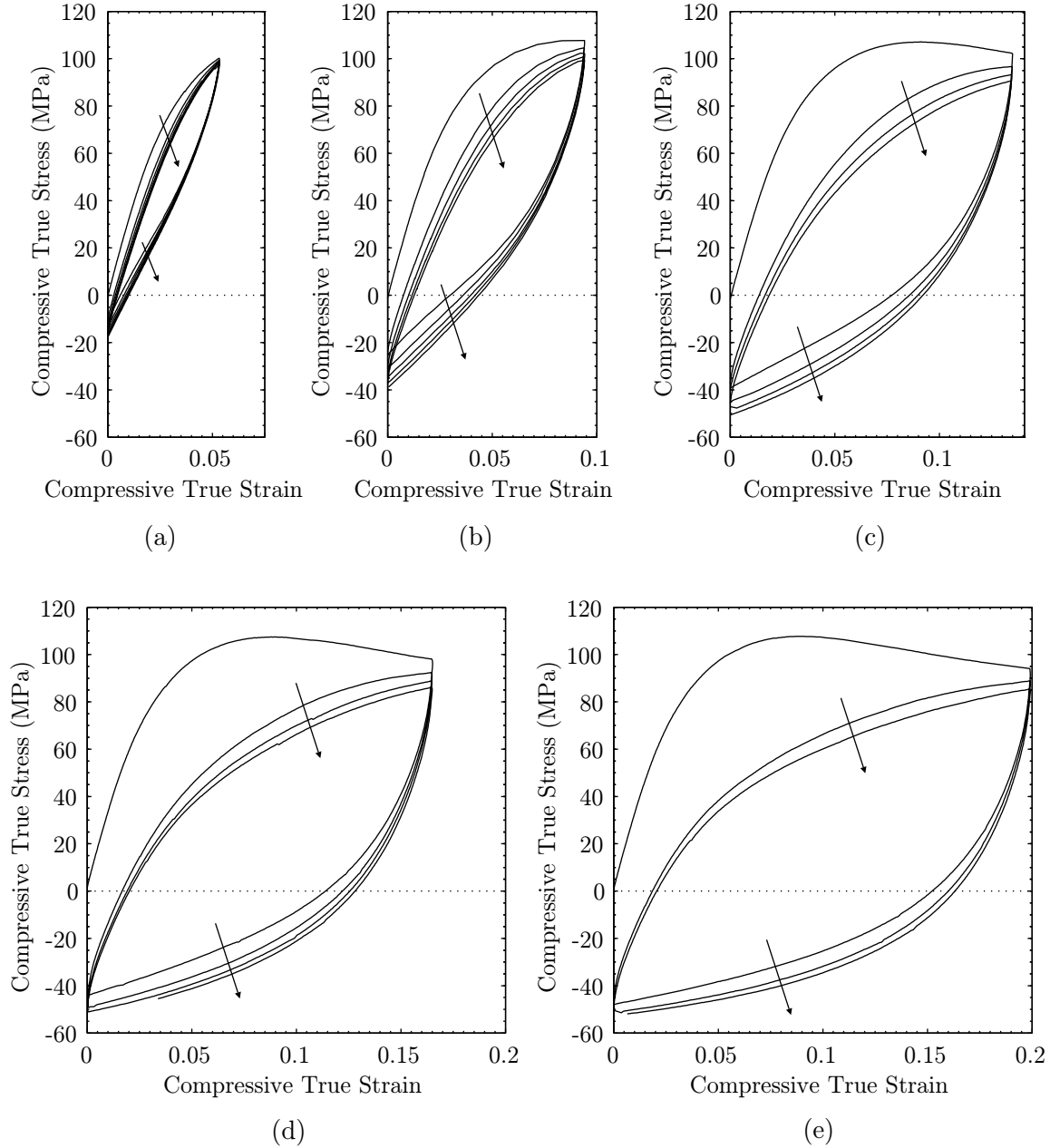
Figure 4-12: Moderate-strain cyclic compression-tension tests on annealed PMMA at room temperature and at a strain rate of -0.0003 s^{-1}. Arrows indicate the direction of movement of the loops as the number of cycles increase. Each specimen was cycled between 0 strain and a compressive strain of (a) -0.053, (b) -0.094, (c) -0.135, (d) -0.165, and (e) -0.199.
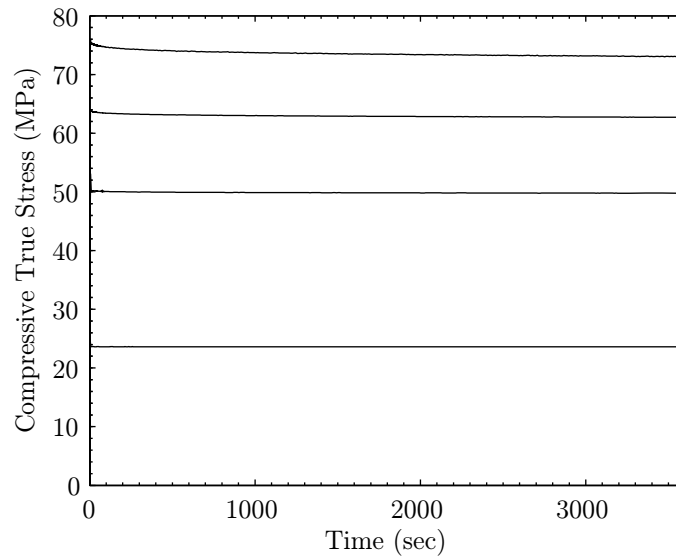
Figure 4-13: Input compressive true stress levels corresponding to creep tests shown in Figure 4-14. Each curve represents a separate specimen. From top to bottom, the tests were conducted at constant force values of 20 kN, 16.5 kN, 13 kN, and 6 kN.
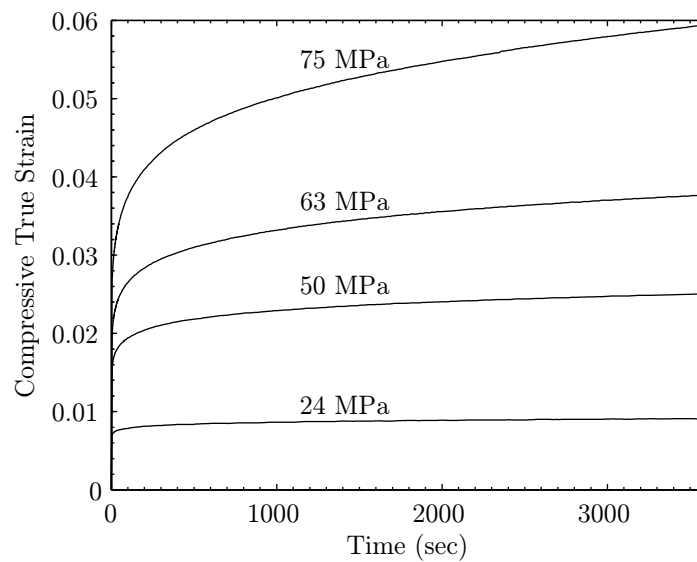
Figure 4-14: Compression creep tests at various pre-yield loads on annealed PMMA at room temperature. Each curve represents a separate specimen.

Chapter 5

Model Parameter Calibration

The first step in calibrating the model is to choose the number of viscoelastic systems N that one would like to represent, while keeping in mind that each viscoelastic system introduces several material parameters, a tensorial internal variable, and a scalar internal variable, which have a flow rule and a backstress equation. Figure 5-1 shows a schematic of the effect of three viscoelastic systems on the stress-strain response. The solid line represents a real compression-tension experiment and the dashed line represents the expected numerical response while using choosing $N = 3$. The $x^{(\alpha)}$ indicate the points on the stress-strain curve where the correspondingly numbered micro-mechanism starts to take effect. The stress level at which each of these systems becomes activated during initial loading is governed by the material parameters $s_i^{(\alpha)}$, and if the internal variables $s^{(\alpha)}$ are chosen to be constant, then the stress level for each system's activation during unloading will be $-2s_i^{(\alpha)}$, measured relative to the stress at the beginning of unloading. The slope that connects the origin to $x^{(1)}$ is governed by the elastic and shear moduli. The slope connecting $x^{(1)}$ and $x^{(2)}$ is governed by $\mu^{(1)}$, the second and third x's by $\mu^{(2)}$, etc. The response after the $x^{(0)}$ is governed by the viscoplastic micro-mechanism, and because it is well known that the yield peak is due to an increase in free volume in the material, we have chosen to use the internal variable φ to represent a measure of the free volume and it will increase as the viscoplastic system is stretched. The yield peak and subsequent softening is then accomplished by allowing $s^{(0)}$ to evolve and coupling it with the evolution of φ.
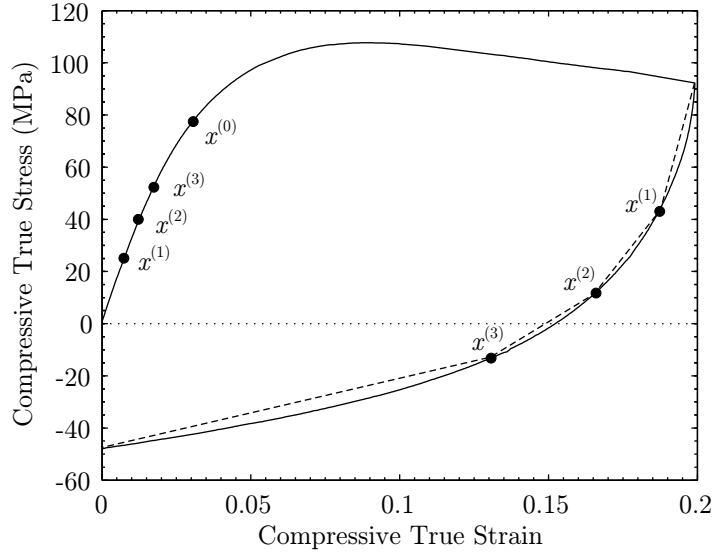
Figure 5-1: Schematic of the effect of the viscoelastic systems on the stress-strain response. The solid line represents an experiment and the dashed line represents the expected numerical response while using choosing $N = 3$. The bold x's indicate the point on the stress-strain curve where the effect of the correspondingly numbered micro-mechanism sets in.

Furthermore, from the experimental results, it can be seen that the $\mu^{(\alpha)}$ corresponding to each of the viscoelastic systems should be reduced considerably by the time a strain of 20% has been reached in order to match the slopes of the unloading response, which is significantly softer than the initial loading response. From the cyclic loading experiments in Figure 4-12, we resolve that the slopes should not continue to soften by much once the first load cycle is complete. We hope to achieve the proper softening of $\mu^{(\alpha)}$ by allowing it to decrease along with any increase in φ.

As can be seen from the schematic in Figure 5-1, choosing only three viscoelastic systems gives a response with very sharp transitions. These transitions may be smoothed a bit by considering the effects of the rate-sensitivity of the flow rule, but noticeable transitions between the systems may still remain. One is inclined to choose a large number of viscoelastic systems, say by setting $N = 100$, in order to provide a very smooth qualitative solution. However, this would also introduce a large number of material constants, internal variables, and constitutive functions that would make the calibration procedure unrealistic and computationally expensive. Therefore, we have chosen to set $N = 3$ so that the list of

material constants, internal variables, and constitutive equations remains reasonable while still obtaining a respectable approximation to the actual stress-strain curve.

5.1   One-Dimensional Procedure

The one-dimensional calibration procedure follows three steps. First we calibrate the loading response, then the unloading response, and finally the creep response. We have chosen to focus on three sets of experimental data for calibration purposes. The first is compression-tension data for strains between 10% and 20%, the second is large strain compression data, and the third is pre-yield creep data. The calibration procedure follows.

1. As a first cut, we calibrate only the loading response of the material, therefore, we ignore the softening of $\mu^{(\alpha)}$, which we assume for now only comes into play upon unloading of the material. In order to accomplish this, we will set $\dot{\mu}^{(\alpha)} = 0$, which eliminates $\mu_{\mathrm{cv}}^{(\alpha)}$ and $c^{(\alpha)}$ from the list of parameters. Furthermore, we make the assumption that the initial values of the viscoelastic $\mu^{(\alpha)}$'s are equivalent since the initial slope is quite linear, hence

$$\mu_i = \mu_i^{(1)} = \mu_i^{(2)} = \mu_i^{(3)} \tag{5.1}$$

Further, we have determined that $\mu^{(0)}$ is reasonably insignificant in the entire fitting procedure, so we choose

$$\mu^{(0)} = \mu_i^{(0)} = \mu_{\mathrm{cv}}^{(0)} = 0 \text{ MPa} \tag{5.2}$$

Also, we approximate the model as rate-independent by choosing $m^{(\alpha)}$ to be a small number such as 0.01. And, we set $\dot{\epsilon}_0 = 0.0003$ in order to match the strain rate of our experiments. We then have a smaller list of 15 parameters that we can try to roughly estimate based solely on the loading response:

$$\left\{ E, \mu_R, \lambda_L, \mu_i, \mu_i^{(0)}, h_0, g_0, b, \varphi_i, \varphi_{\mathrm{cv}}, s_{\mathrm{cv}}^{(0)}, s_i^{(\alpha)} \right\} \tag{5.3}$$

A schematic showing the regions where a particular parameter dominantly affects the stress-strain loading response is shown in Figure 5-2. By examining the initial portion
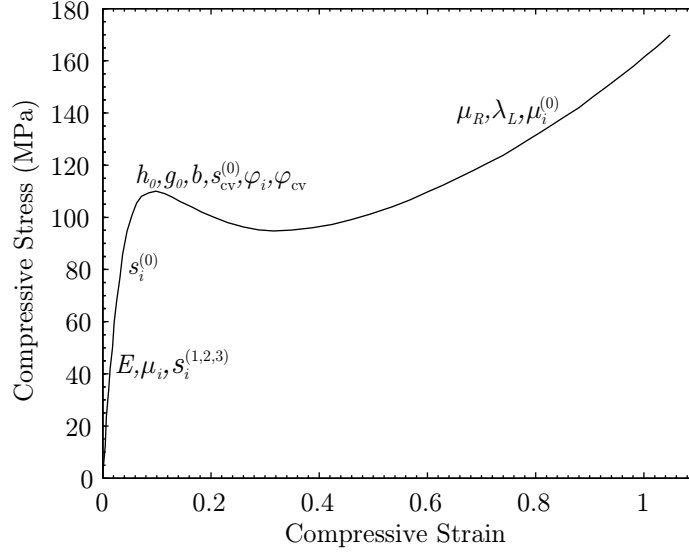
Figure 5-2: Schematic of the effect of various material parameters on different regions of the stress-strain loading response for the one-dimensional model.

of the experimental stress-strain curve, we easily determine the Young's modulus E as well as an approximate value for μ_i. We cannot yet determine particular values for $s_i^{(1,2,3)}$, but we can determine a range in which they should lie; equally spaced somewhere between 20 MPa and 60 MPa. We choose $s_i^{(0)}$ to be at the point where the stress-strain response starts to significantly deviate from linearity; somewhere around 80 MPa. In summary, we want

$$s_i^{(1)} < s_i^{(2)} < s_i^{(3)} < s_i^{(0)} \tag{5.4}$$

From Gearing (2002), we choose μ_R and λ_L to be close to 10 MPa and 1.5 respectively. Decrementing μ_R or incrementing λ_L will soften the large-strain behavior, and the opposite is true for creating a stiffer large-strain response. Given these assumptions, the only parameters that remain are those that correspond to the evolution of the free volume and the evolution of $s^{(0)}$, which together control the shape of the yield peak. We then make one final assumption by choosing $\varphi_i = 0$, and assume this relates to the virgin state of the material so that any changes in free volume will be measured relative to this initial state.
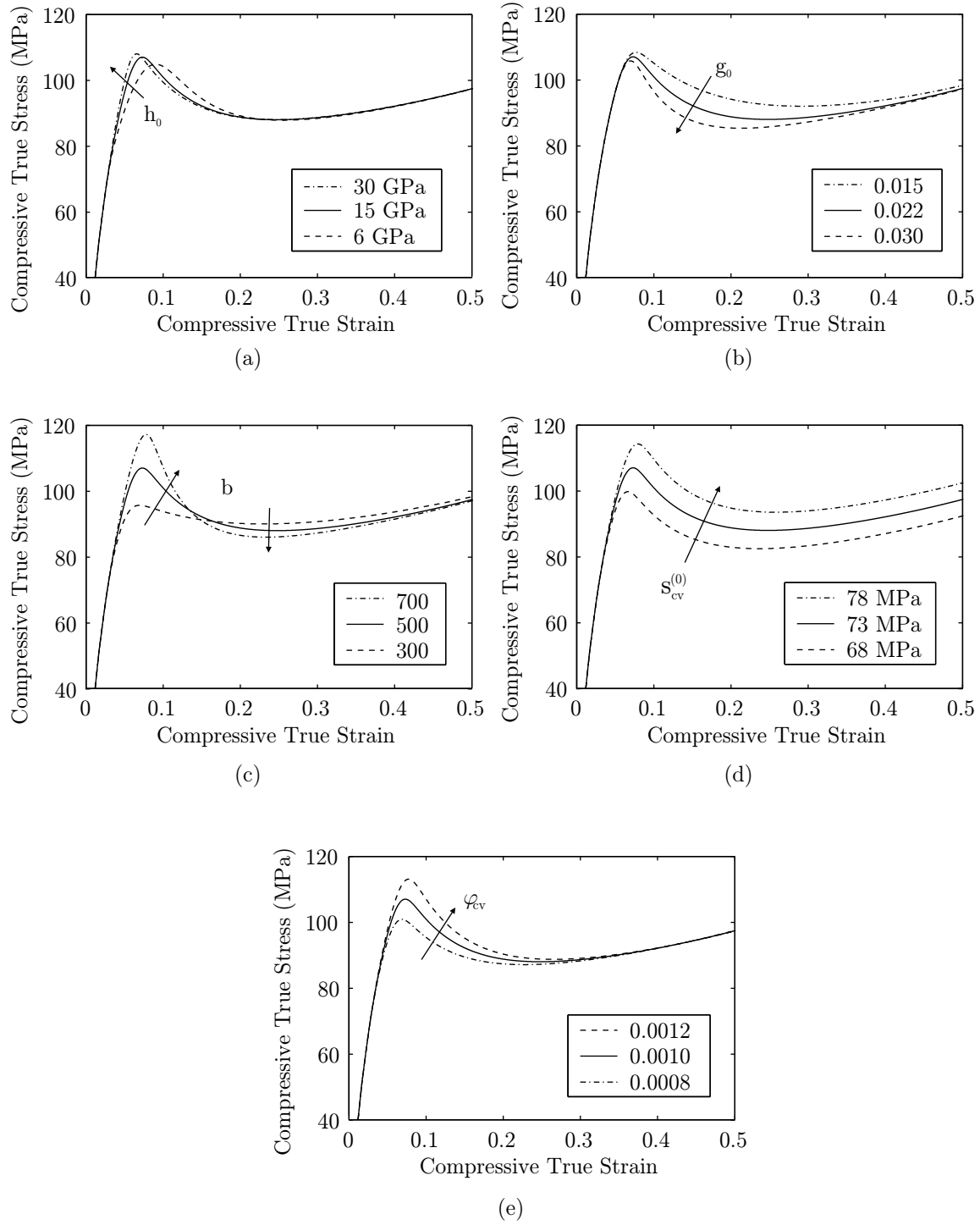
Figure 5-3: Schematic of the effect of various material parameters on the shape of the yield peak. Arrows indicate an increase in the parameter (a) h_0 (b) g_0 (c) b (d) $s_{cv}^{(0)}$ (e) φ_{cv}.

Several iterations must be performed to obtain the correct shape for the yield peak, but Figure 5-3 can be used as a guideline for visualizing how changing the various parameters can affect the shape of the peak. The actual values shown are less important than knowing how the curve will move when a parameter is incremented or decremented. By inspecting the figures, we see that h_0 is the only parameter that affects the pre-peak slope, and the remaining parameters affect later portions of the curve. It can also be seen that the effect on the stress-strain response induced by any change in φ_{cv} may also be accomplished by changing b and g_0 together, hence to simplify matters we can fix $\varphi_{cv} = 0.001$. Finally, it is clear that changes in $s_{cv}^{(0)}$ simply shift the region up and down, which is a simple method to fine-tune the stress-level of the post-yield minimum. Guided with this information, one can iterate to estimate a possible combination of parameters to roughly fit the loading response. It is not important to get a perfect fit on this first cut, as further calibration procedures will require these parameters to be adjusted further.

2. Now, we consider fitting the unloading response by finding reasonable values for $c^{(\alpha)}$ and $\mu_{cv}^{(\alpha)}$, which determine the rate of softening and the final value of $\mu^{(\alpha)}$ respectively. As can be seen from Figure 5-1, and keeping in mind that $\mu^{(\alpha)}$ is a stiffness, we want

$$\mu_{cv}^{(1)} > \mu_{cv}^{(2)} > \mu_{cv}^{(3)} \tag{5.5}$$

And it follows from our equation for the evolution of $\mu^{(\alpha)}$

$$\dot{\mu}^{(\alpha)} = c^{(\alpha)} \left(1 - \frac{\mu^{(\alpha)}}{\mu_{cv}^{(\alpha)}} \right) \dot{\varphi} \tag{5.6}$$

and assuming the set of $\dot{\mu}^{(\alpha)}$ are nearly equivalent, that

$$c^{(1)} > c^{(2)} > c^{(3)} \tag{5.7}$$

It is useful at this point to plot the evolution of $\mu^{(\alpha)}$ with strain in addition to the stress-strain curve in order to verify that the proper softening rates for $\mu^{(\alpha)}$ are being obtained. One should pick a strain level at which $\mu^{(\alpha)}$ should reach $\mu_{cv}^{(\alpha)}$ and choose

$c^{(\alpha)}$ in order to obtain that goal. One note of caution, if $c^{(\alpha)}$ is set too high, then it can severely alter the evolution of φ and produce undesirable artifacts on the resulting stress-strain curve. In any case, with several iterations one can find a reasonable fit for the unloading response by finding appropriate values for $s_i^{(\alpha)}$, $c^{(\alpha)}$, and $\mu_{\text{cv}}^{(\alpha)}$. Keep in mind that this may require one to alter the values found while calibrating the loading response in the previous step.

3. As a final step, we can estimate the rate-sensitivity parameters $m^{(\alpha)}$. One approach is to calibrate the model with experimental creep results. It is difficult to outline a procedure, but it has been found that a reasonable fit can be obtained by assuming that

$$m = m^{(1)} = m^{(2)} = m^{(3)}. \tag{5.8}$$

For PMMA, it has been found that these are greater than the rate-sensitivity parameter for the viscoplastic system. In summary

$$m > m^{(0)} \tag{5.9}$$

Once values for m and $m^{(0)}$ have been determined, further iterations must be performed until the loading, unloading, and creep responses are calibrated satisfactorily with the available experimental data.

Following the one-dimensional calibration procedure outlined above with some of the experimental data presented in Chapter 4, the following material parameters for PMMA were

found:

$$E = 4.2 \text{ GPa} \qquad \mu_R = 17 \text{ MPa} \qquad \lambda_L = 1.7 \qquad \dot{\epsilon}_0 = 0.0003$$

$$\mu_i = 3.5 \text{ GPa} \qquad \mu_{\text{cv}}^{(1)} = 1.1 \text{ GPa} \qquad \mu_{\text{cv}}^{(2)} = 0.4 \text{ GPa} \qquad \mu_{\text{cv}}^{(3)} = 0.2 \text{ GPa}$$

$$s_i^{(0)} = 77 \text{ MPa} \qquad s_i^{(1)} = 26 \text{ MPa} \qquad s_i^{(2)} = 43 \text{ MPa} \qquad s_i^{(3)} = 61 \text{ MPa}$$

$$s_{\text{cv}}^{(0)} = 62 \text{ MPa} \qquad c^{(1)} = 4.5 \text{ GPa} \qquad c^{(2)} = 1.8 \text{ GPa} \qquad c^{(3)} = 1.3 \text{ GPa}$$

$$\varphi_i = 0 \qquad \varphi_{\text{cv}} = 0.001 \qquad h_0 = 12 \text{ GPa} \qquad g_0 = 0.012$$

$$b = 850 \qquad m^{(0)} = 0.085 \qquad m = 0.17$$

Comparisons of the Matlab simulations with the large-strain compression data is shown in Figure 5-4. This data was used to calibrate the loading response. Comparisons with moderate strain compression-tension data is shown in Figure 5-5. The unloading experimental results shown here for 20% strain were used to calibrate the unloading response of the material. As can be seen, the unloading response for 13.5% and 16.5% as well as the large strain unloading are matched well as a result. However, once the data transitions into the tension region (shown here as a negative stress), the model tends to deviate from the data quite significantly. Yet, with an application towards indentation in mind, where the tension response is irrelevant, we consider this part of the data to be somewhat of a minor concern. And finally, comparison with creep data is shown in Figure 5-6. The fit was obtained by iterating through m and $m^{(0)}$ until all four curves were reasonably well represented.
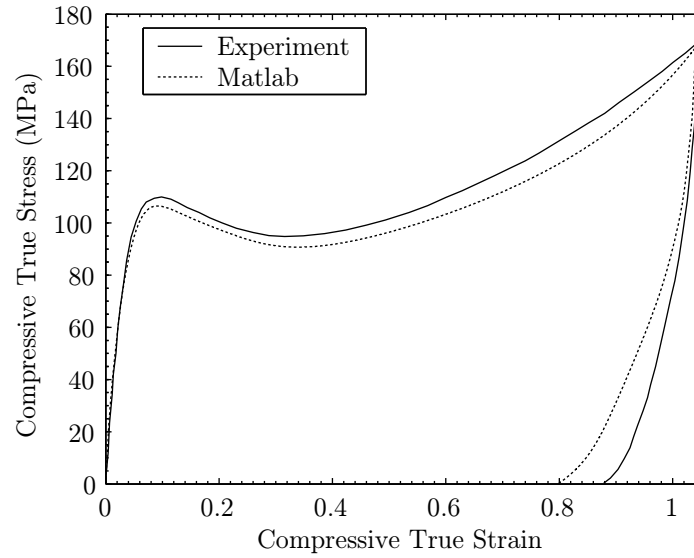
Figure 5-4: Large-strain compression experiment versus Matlab simulation. A reasonable fit has been obtained for both the loading and unloading responses.
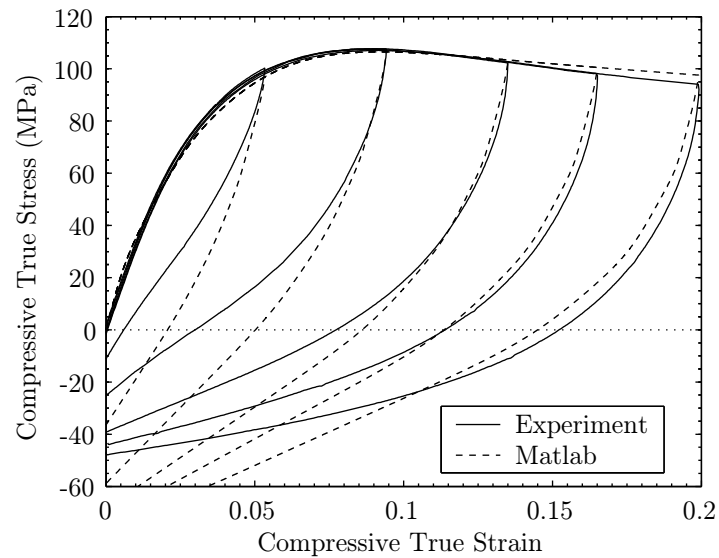

Figure 5-5: Compression-tension experiments versus Matlab simulations. Reasonable fits have been obtained for all but the experiments to a maximum strain of 5.3% and 9.4%.
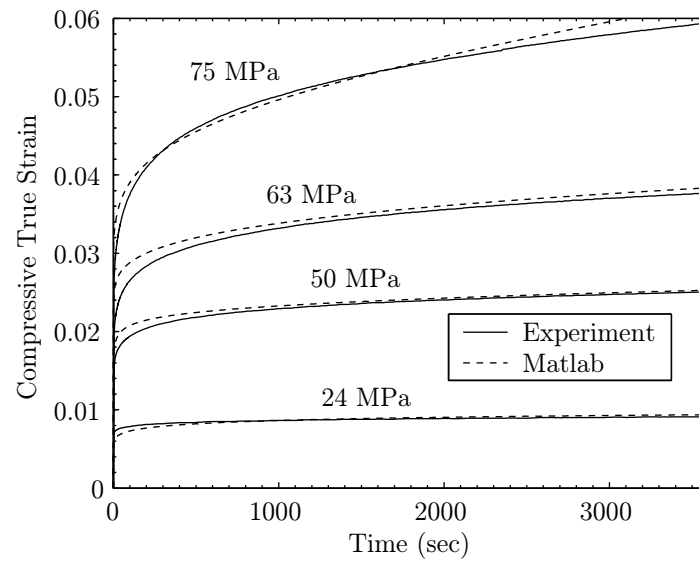
Figure 5-6: Creep experiments versus Matlab simulations. Reasonable fits have been obtained for the three lower stress levels. The curvature is not as well represented by the 75 MPa simulation.

5.2 Three-Dimensional Procedure

Following our assumptions from the one-dimensional calibration procedure, the list of 28 material parameters that are necessary for the three-dimensional model when $N = 3$ is:

$$\left\{ G, K, \mu_R, \lambda_L, \mu_i, c^{(\alpha)}, \mu_{\text{cv}}^{(\alpha)}, \nu_0, m^{(0)}, m, h_0, g_0, b, \varphi_i, \varphi_{\text{cv}}, s_{\text{cv}}^{(0)}, s_i^{(\alpha)}, \alpha_p^{(\alpha)} \right\} \tag{5.10}$$

Our hope is that these parameters can be easily estimated based on the results of the one-dimensional calibration process, and that minimal further iterations are necessary to account for differences due to pressure sensitivity and volume changes, neither of which are represented in the one-dimensional model.

Before we can compare the two versions of the model, we must first convert the one-dimensional parameters to shear values to be used in the three-dimensional model. To accomplish this, we need to enforce these equalities

$$\tau^{(\alpha)} \nu^{(\alpha)} = \sigma^{(\alpha)} \dot{\epsilon}^{(\alpha)}, \tag{5.11}$$

$$\sigma^{(\alpha)} = \sqrt{3} \tau^{(\alpha)}, \tag{5.12}$$

which also implies

$$\dot{\epsilon}^{(\alpha)} = \frac{\nu^{(\alpha)}}{\sqrt{3}}. \tag{5.13}$$

This leads to the conclusion that all of the one-dimensional material parameters are unchanged in the shear form except for the list of parameters $\{\dot{\epsilon}_0, s_0^{(\alpha)}, s_{\text{cv}}^{(0)}, h_0\}$ which may be converted as follows

$$\left. \begin{aligned} \dot{\epsilon}_0 &= \tfrac{1}{\sqrt{3}} \nu_0, \\ s_0^{(\alpha)\text{tension}} &= \sqrt{3} s_0^{(\alpha)\text{shear}}, \\ s_{\text{cv}}^{(0)\text{tension}} &= \sqrt{3} s_{\text{cv}}^{(0)\text{shear}}, \\ h_0^{\text{tension}} &= 3 h_0^{\text{shear}}. \end{aligned} \right\} \tag{5.14}$$

Now, if we assume a Poisson ratio of 0.33, the list of parameters necessary for the three-dimensional model is nearly complete, we simply need to find the pressure-sensitivity parameters $\alpha_p^{(\alpha)}$; we will choose a previously published value of $\alpha_p = 0.204$ (Rabinowitz as

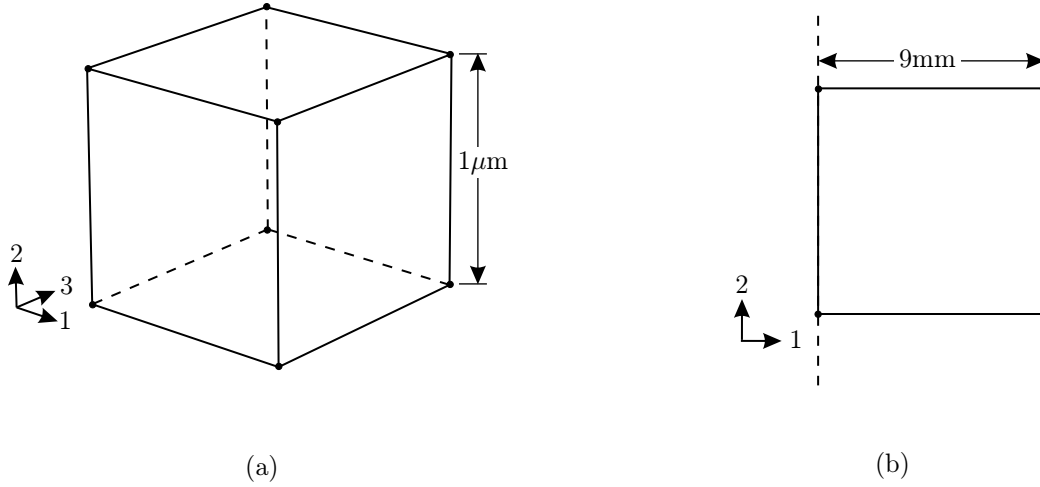(a)   (b)

Figure 5-7: Schematic of Abaqus elements used for simulations. (a) Continuum three-dimensional eight-node element with reduced integration (C3D8R) and 1 micrometer edge length used for displacement controlled experiments. (b) continuum axisymmetric four-node element with reduced integration (CAX4R) with an edge length of 9 mm.

cited in Gearing, 2002) such that

$$\alpha_p^{(\alpha)} = \alpha_p = 0.204 \tag{5.15}$$

Two different input files were created for the Abaqus simulations depending on the loading situation desired. For displacement controlled compression-tension simulations, a single square continuum three-dimensional eight-node element with reduced integration (C3D8R) and 1 micrometer edge length was used as shown in Figure 5-7.a. A velocity profile that equated to constant true strain was applied to the top surface of the element in the 2 direction. The bottom surface of the element was free to move in the 1-3 plane, except for one node on the bottom which was fixed in all degrees of freedom. For load controlled creep simulations, a single continuum axisymmetric four-node element with reduced integration (CAX4R) with an edge length of 9 mm was used as shown in Figure 5-7.b. The radius was chosen to be identical to the compression-tension specimen used in the experiments. A rigid plate was used to apply the same loading profile as used in the experiments to the top edge of the element. The left edge was free to move in only the 2 direction. The bottom edge was free to move in only the 1 direction.
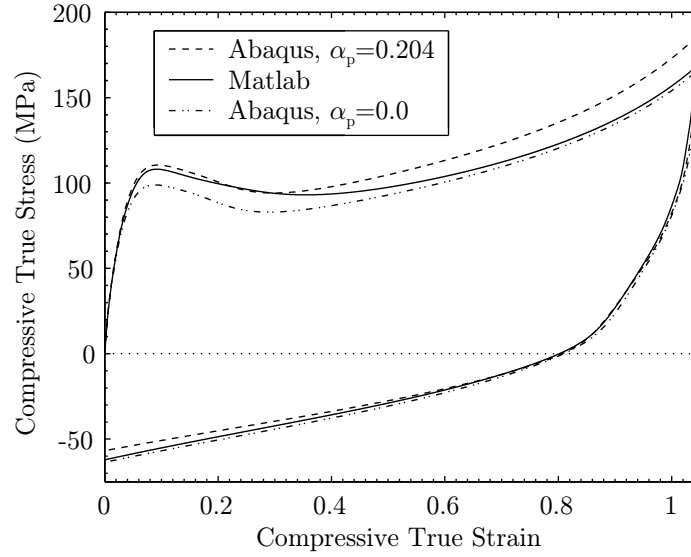
Figure 5-8: Comparison of Abaqus and Matlab simulations with same material parameters. Abaqus simulations shown with and without the pressure-sensitivity parameter.

Figure 5-8 compares the large-strain compression-tension results of a Matlab simulation with two Abaqus simulations using the same material parameters that have been converted as necessary according to (5.14). The two Abaqus cases illustrate the effect of the pressure-sensitivity parameter, one case is with $\alpha_p = 0.0$ and the other with $\alpha_p = 0.204$. As can be seen, neither Abaqus simulation is identical to the Matlab simulation, in fact, the Matlab simulation tends to approach the $\alpha_p = 0.204$ case at small strains, and the $\alpha_p = 0.0$ case at larger strains. However, it is clear that the Matlab calibration procedure does provide material parameters that are very close approximations to the ones needed for the three-dimensional model in Abaqus.

In the end, only a few more iterations were required with Abaqus to slightly modify the values of μ_R and b in order to bring the Abaqus simulation into close agreement with the experimental data. The complete list of parameters used for the three-dimensional

shear-yielding model are:

$$G = 1.58 \text{ GPa} \qquad K = 4.12 \text{ GPa} \qquad \mu_\text{R} = 15 \text{ MPa} \qquad \lambda_\text{L} = 1.7$$

$$\mu_i = 3.5 \text{ GPa} \qquad \mu_\text{cv}^{(1)} = 1.1 \text{ GPa} \qquad \mu_\text{cv}^{(2)} = 0.4 \text{ GPa} \qquad \mu_\text{cv}^{(3)} = 0.2 \text{ GPa}$$

$$s_i^{(0)} = 45 \text{ MPa} \qquad s_i^{(1)} = 15 \text{ MPa} \qquad s_i^{(2)} = 25 \text{ MPa} \qquad s_i^{(3)} = 35 \text{ MPa}$$

$$s_\text{cv}^{(0)} = 36 \text{ MPa} \qquad c^{(1)} = 4.5 \text{ GPa} \qquad c^{(2)} = 1.8 \text{ GPa} \qquad c^{(3)} = 1.3 \text{ GPa}$$

$$\nu_0 = 0.0005 \qquad h_0 = 4 \text{ GPa} \qquad g_0 = 0.012 \qquad b = 850$$

$$\varphi_i = 0 \qquad \varphi_\text{cv} = 0.001 \qquad m^{(0)} = 0.085 \qquad m = 0.18$$

$$\alpha_\text{p} = 0.204$$

Comparisons of the Abaqus simulations with the large-strain and moderate-strain compression data is shown in Figures 5-9 and 5-10, respectively. The results are very similar to those obtained using Matlab earlier. Once again, the model is fit reasonably well in the compression region for strains greater than about 10%.

Figures 5-11 and 5-12 compare moderate-strain cyclic compression-tension data with Abaqus simulations. The top figures are experiments, with the corresponding simulation immediately below. Arrows on the figures indicate the direction of movement of the loops as the number of cycles increases. This experimental data was not used in the calibration procedure, yet it is clear that the simulation is capable of picking up the features of cyclic loading in these ranges.

And finally, Figure 5-13 compares compressive creep experiments with Abaqus simulations. The amount of creep and the approximated curvature of the strain-time line is reasonably well fit with Abaqus. In addition, Figure 5-14 compares the strain recovery experiment to 20% strain with the Abaqus simulation. Because this data is on a shorter time scale than the creep experiments, it was used to fine tune the rate sensitivity parameter m which corresponds to the viscoelastic micromechanisms.

As a final note, Figures 5-15, 5-16, and 5-17 show the evolution of φ (the free volume internal variable), $\mu^{(\alpha)}$, and $s^{(0)}$, respectively, up to a strain of 0.5. As can be seen, φ smoothly increases until saturating at φ_cv. Also, it is clear that $\mu^{(\alpha)}$ and $\tilde{s}^{(0)}$ smoothly decrease in proportion to an increase of φ. Furthermore, the resulting evolution of $s^{(0)}$, first

to a peak and then the subsequent softening, clearly illustrates how we obtained the final shape of the stress-strain curve.
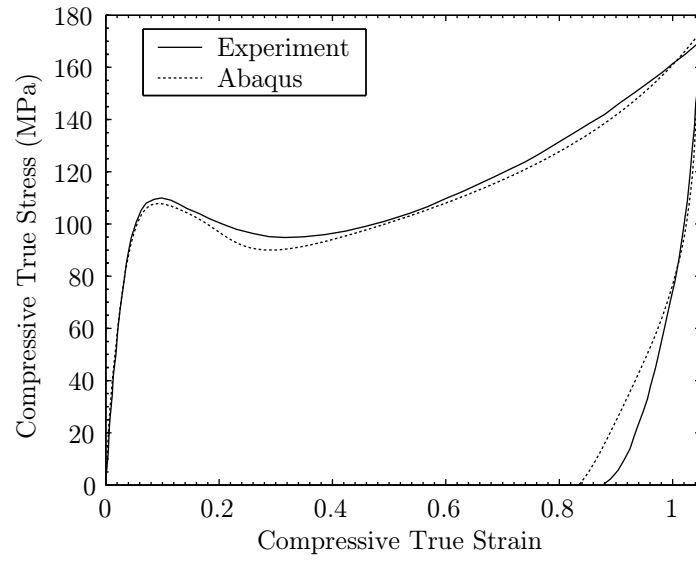
Figure 5-9: Large-strain compression experiment versus Abaqus simulation.
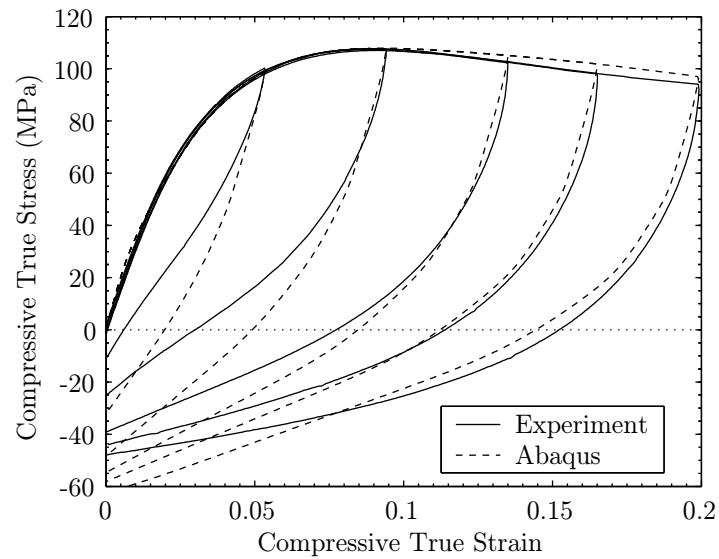

Figure 5-10: Compression-tension experiments versus Abaqus simulations at a strain rate of 0.0003 s^{-1}. Each curve represents a separate specimen.

Figure 5-11: Cyclic compression-tension (a-c) experiments versus (d-f) Abaqus simulations at a strain rate of 0.0003 s^{-1}. Each curve represents a separate specimen. Arrows on the figures indicate the direction of movement of the loops as the number of cycles increases
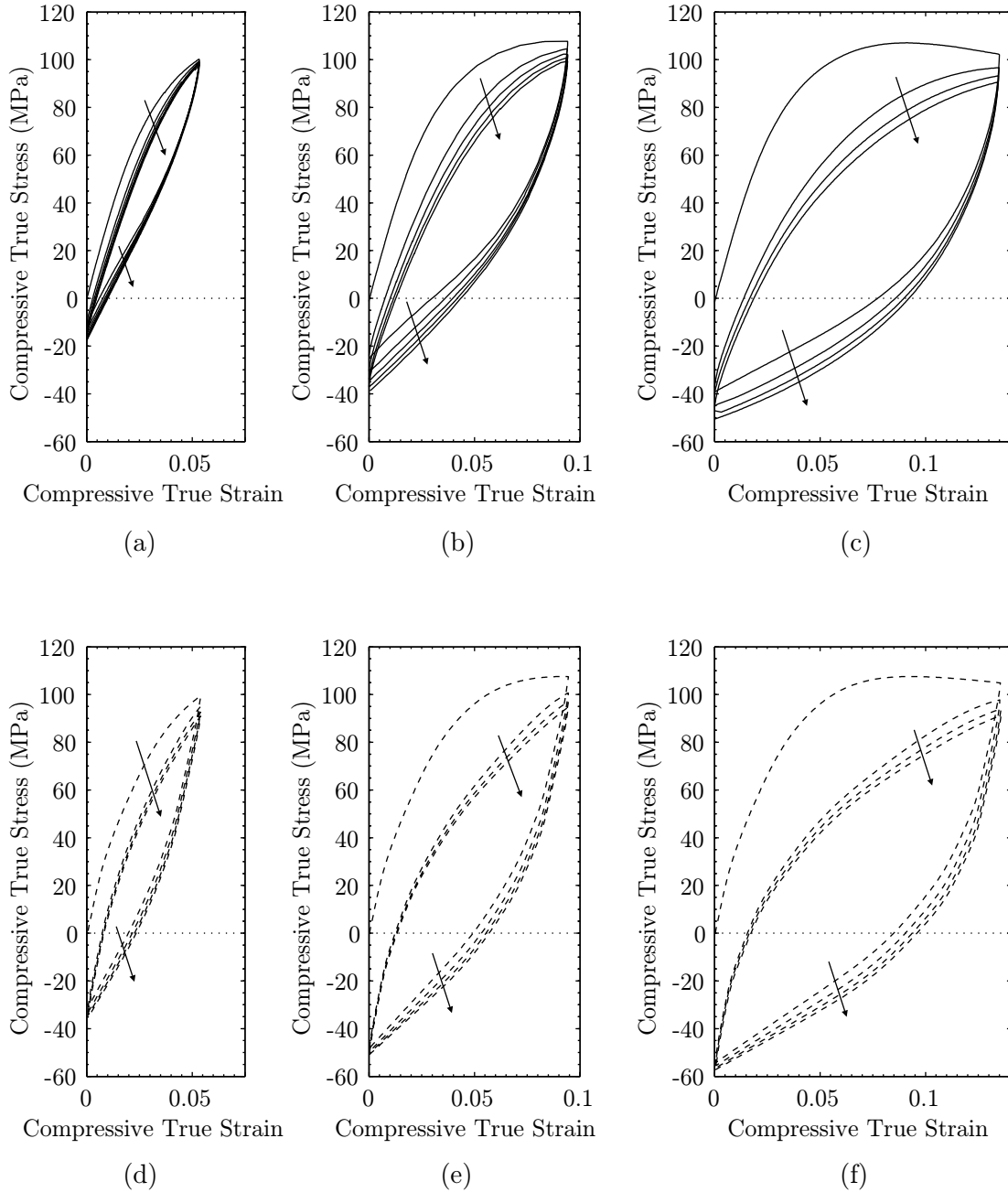
Figure 5-12: Cyclic compression-tension (a-b) experiments versus (c-d) Abaqus simulations at a strain rate of 0.0003 s^{-1}. Each curve represents a separate specimen. Arrows on the figures indicate the direction of movement of the loops as the number of cycles increases
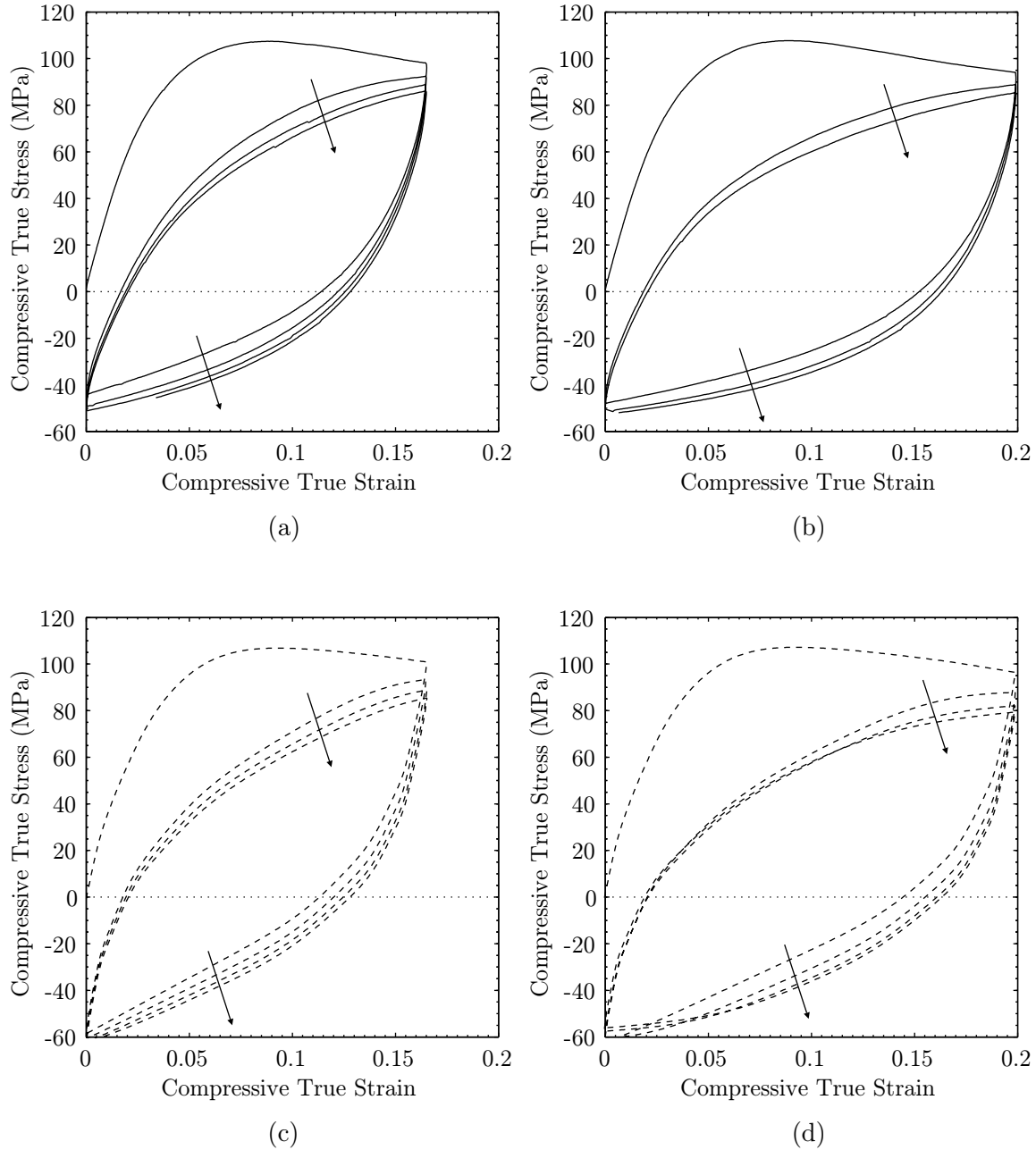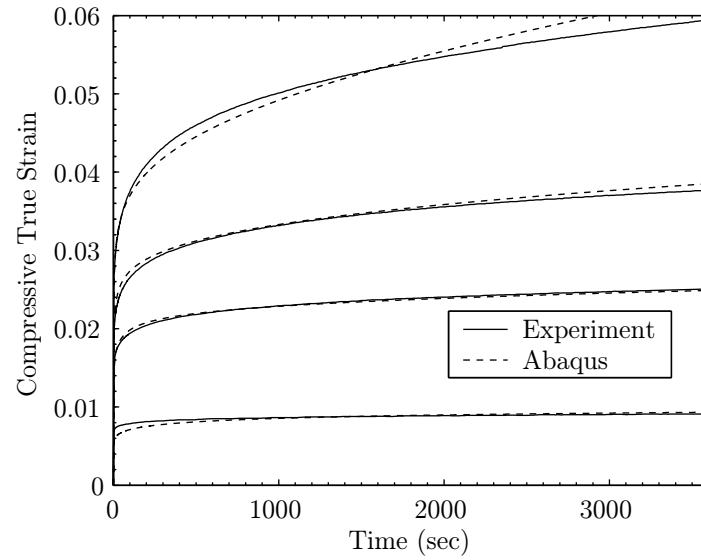
Figure 5-13: Creep experiments versus Abaqus simulations. Each curve represents a separate specimen.

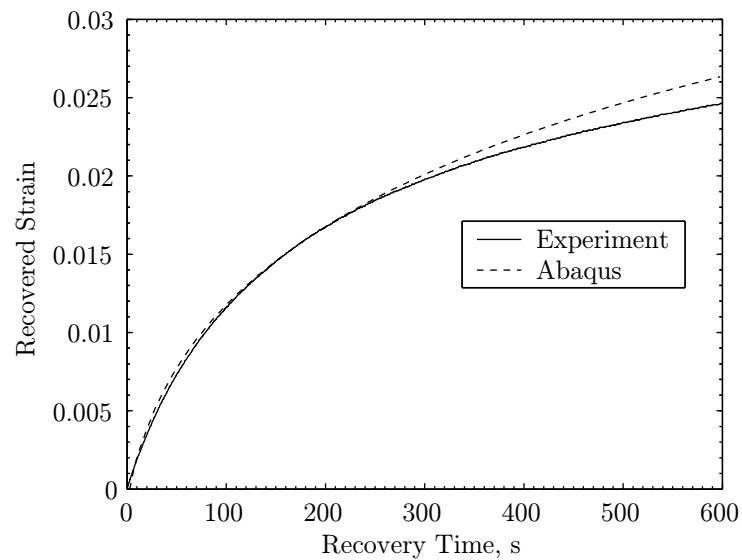Figure 5-14: Strain recovery experiments versus Abaqus simulations. Each curve represents a separate specimen.
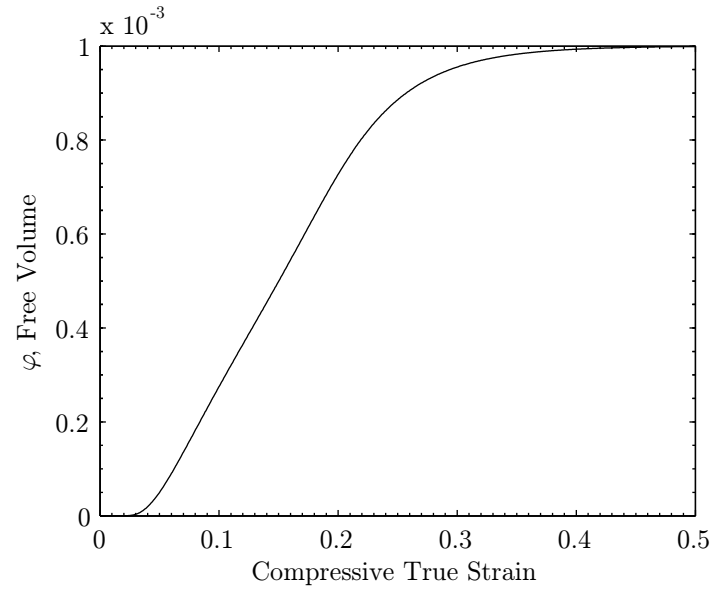
Figure 5-15: Evolution of φ (free volume) with true strain for Abaqus simulation .
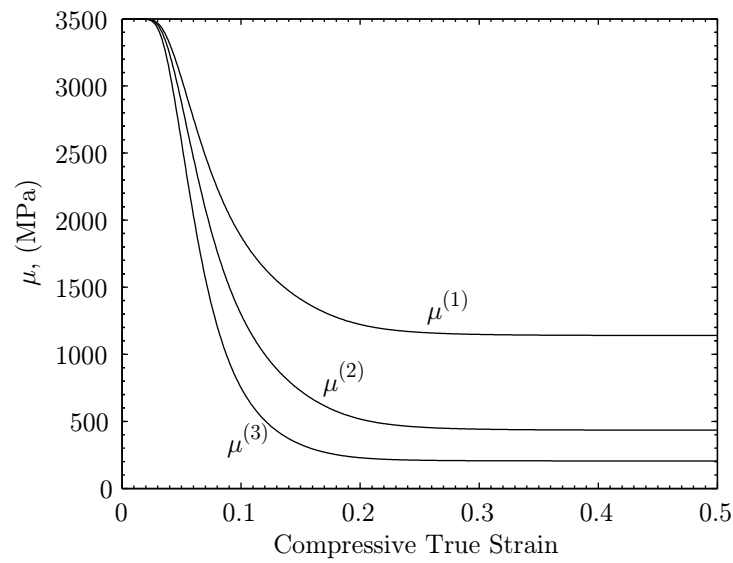

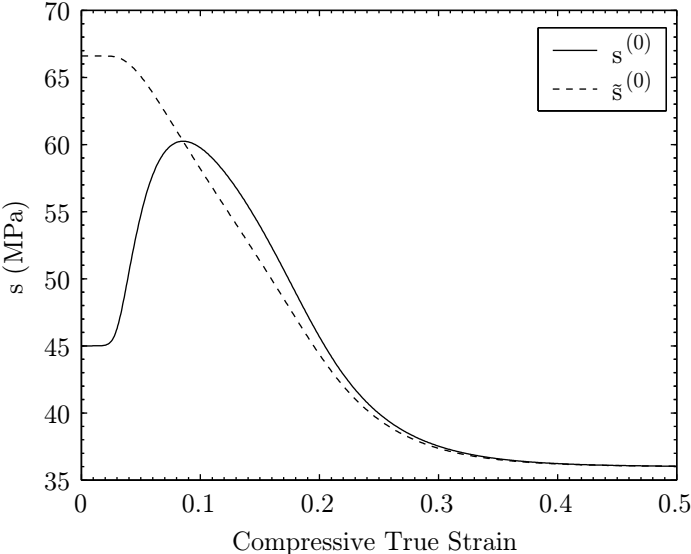Figure 5-16: Evolution of $\mu^{(\alpha)}$ ($\alpha = 1, 2, 3$) with true strain for Abaqus simulation.

Figure 5-17: Evolution of $s^{(0)}$ and $\tilde{s}^{(0)}$ with true strain for Abaqus simulation .

Chapter 6

Application to Microindentation

Indentation experiments have been used for years to quickly extract material parameters from materials in a non-destructive manner. Briefly, an indentation experiment involves driving a rigid object with known shape into a material while recording the object's force-depth profile, or 'P-h curve'. These tests may be conducted in either force or displacement control, where the choice between the two methods is usually dependent on the design of the testing apparatus. The depths of penetration for these tests can range from the nanometer to the millimeter scale, which is dependent on both the resolution of the testing apparatus as well as the quantity of material that is available. The results presented here are for tests in the micrometer depth range, and thus they will be referred to as *micro*indentation experiments.

Some of the earliest and still widely used methods for estimating the hardness and Young's modulus of materials from micro and nanoindentation tests were developed by Doerner and Nix (1986) and Oliver and Pharr (1992). While there is presently extensive experimental indentation work on polymeric materials (e.g. Briscoe, Fiori, & Pelillo, 1998; Briscoe & Sebastian, 1996; Ion, Pollock, & Roques-Carmes, 1990; Van Landingham, Villarrubia, Guthrie, & Meyers, 2001; van Melick, Bressers, den Toonder, Govaert, & Meijer, 2003), most indentation numerical analysis work has focused only on metallic materials. Recently, Gearing (2002) performed a detailed numerical analysis on the microindentation of PMMA, polycarbonate, and polystyrene and developed a method to extract the Young's modulus, flow strength, rate sensitivity parameter, and pressure sensitivity parameter for

an elastic-perfectly plastic type constitutive model from a material's P-h curve. The work presented here only attempts to better predict the microindentation response of PMMA in comparison with Gearing's work, and serve as a verification of the quality of our model for engineering applications. A method to extract material parameters for our model from indentation is left as future work.

6.1 Experimental Apparatus and Procedure

The specimen used for these indentation experiments was cut from the same cast PMMA stock as that used for the macro-scale experiments presented in Chapter 4. One face of a 1" diameter disk of approximately 50 mm thickness was polished using 1.0 μm, 0.3 μm, and finally 0.05 μm Alumina suspensions. The specimen was annealed before and after the polishing process. Because thousands of individual indents may be performed on a specimen of this size, only one specimen was needed. All tests were repeated at least 5 times to ensure repeatability of results.

All indentation experiments were performed with the indentation apparatus developed and used by Gearing (2002). The load resolution of the device is 80 μN over a range of 8 N. Displacement resolution is approximately 20 nm over a range or 1.25 mm. All data acquisition takes place on a PC using Labview and a National Instruments PCI card. Raw data was sampled at 1 kHz, however, Labview performed real time averaging before recording data, resulting in a smoothed output with an artificial sampling rate of 10 Hz. The same computer was used to simultaneously control the force of the indenter's voice coil actuator.

There are a variety of standard indentation tips to choose from, and they all usually fall into three categories: cylindrical, spherical, pyramidal, and conical. Briscoe, Sebastian, and Adams (1994) have conducted work comparing these different indenter geometries for polymeric materials.In the present work, we have chosen to use a diamond conical indenter with a half-cone angle of 70.3°, because the simple geometry is easy to model numerically. The particular angle was chosen because it corresponds to the equivalent cone angle of
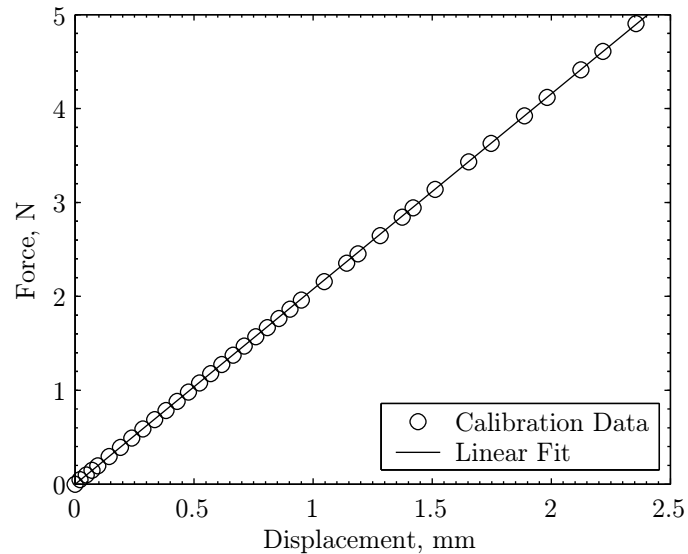
Figure 6-1: Indenter spring stiffness calibration showing a spring constant of 2.0788 N/mm.

a Berkovich indenter tip. A comparison of the P-h curves obtained from each of these geometries will be presented.

6.1.1 Specimen Fixturing

It is imperative that the specimen be securely attached to the stage. In this work, all experiments were conducted using Scotch double-stick tape to attach the specimen to the stage. It was found that by allowing the specimen to rest freely on the stage, large errors in displacement measurements were recorded. In the future it may be important to develop a permanent mechanical fixture that attaches the specimen to the stage.

6.1.2 Flexure Stiffness Measurements

The stiffness of the indenter flexure mechanism was verified throughout the range of 0 to 5 N using a set of precision masses. Figure 6-1 shows the results of the calibration along with a linear fit of the data. The flexure stiffness was found to be 2.0788 N/mm.
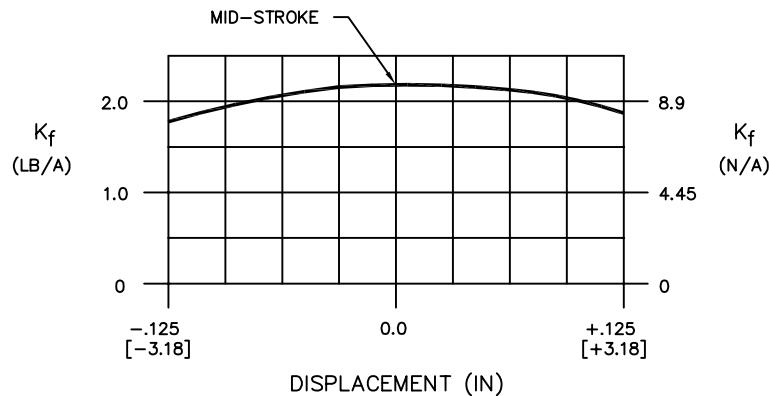
Figure 6-2: Voice coil force constant as a function of its stroke. (BEI, Kimco Magnetics Division, 1994)

6.1.3 Voice Coil Characterization

In earlier work (Gearing, 2002), it was assumed that the voice coil and accompanying electronics behaved linearly throughout their ranges. However, this is not always true. First of all, as shown in the documentation provided by the voice coil manufacturer in Figure 6-2, the factor which relates the voice coil's current draw to the force it exerts is not constant throughout its stroke. Therefore, only at displacements very close to the mid-stroke of the voice coil can we assume that the force-current relationship of the voice coil is linear. Furthermore, it was found that the force constant of the voice coil is also dependent on its temperature. When the voice coil is driven with a relatively high current of about 1 A, which corresponds to a force of approximately 4 N, the temperature of the voice coil increased from 21 C to 38 C in 15 minutes. This results in an increased resistance in the voice coil wires and thus reduces the voice coil's force constant. In addition, because the voice coil is not thermally isolated from the indenter frame, the temperature of the frame between the voice coil and the indenter tip was shown to increase to approximately 30 C over this same time frame. However, at a driving current of approximately 0.25 A, which corresponds to a force of approximately 1 N, the voice coil was found to increase to a temperature of only about 27 C and the heating of the indenter frame was less noticeable. In order to avoid the voice coil's non-linearities and thermal effects, all indentation experiments presented here were conducted by insuring that the voice coil travelled no more than about 50 μm from its

mid-stroke before making contact with the specimen, and all force levels were kept below 1 N.

6.1.4 Apparatus Compliance Measurements

Prior to this work, an adequate method for measuring the compliance of the indenter load frame had not been recorded. Oliver and Pharr (1992) documented an extensive calibration procedure for indentation apparatuses that simultaneously measured the indenter frame compliance as well as the indenter tip area function. Their method involves analyzing over one hundred indents, but this can be an extraordinarily time consuming effort, so a slightly cruder attempt to find the compliance of the indenter was employed. The indenter tip was removed from the apparatus, and the blunt apparatus was then driven into a block of hardened tool steel which had been secured to the indenter stage with Scotch double-stick tape. Assuming that the steel is rigid compared to the aluminum indenter frame, any measured displacements after contact occurs is assumed to be due to the compliance of the indenter frame and the double-stick tape. Figure 6-3 shows the results of such an experiment with three consecutive load/unload cycles. The loading portion of the first cycle is slightly more compliant than the others, which is most likely due to the initial seating of the steel block and tape against the stage. From the subsequent cycles, a compliance of approximately 0.7 μm/N was measured. This value will be used to adjust the conical indentation experimental data for PMMA.

6.1.5 Zero Offset

Another correction that has been applied to the indentation experimental data is a zero offset for the depth measurements. Typical raw experimental data is shown in Figure 6-4. Initially, there is a linear region before the indenter has made contact. Then there is a sharp rise in the force once contact has occurred. However, due to lags in the system, and the limited data sampling frequency, as well as the limited resolution of the displacement sensors, the actual contact point may differ from the one determined from the data. To correct for this uncertainty, the experimental P-h curves may be shifted by as much as $\pm 1\mu$m to ensure that the loading curvature of each experiment is consistent for a given
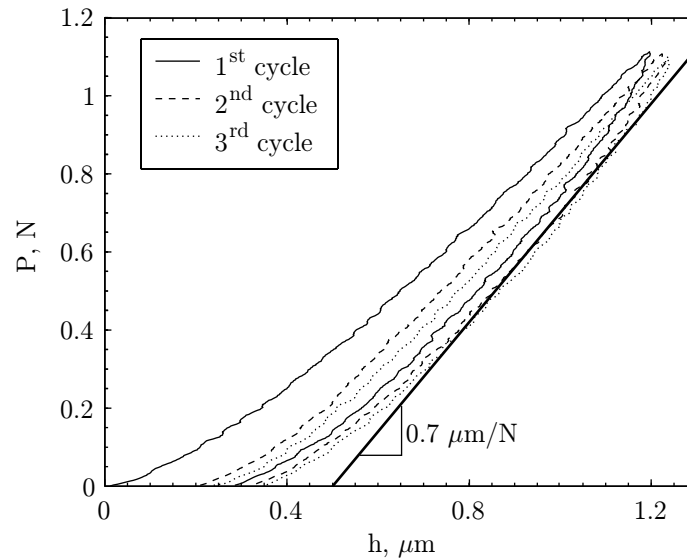
Figure 6-3: Measured compliance with blunt indenter for three consecutive load/unload cycles on block of hardened tool steel.

material and loading rate. It is important to note that this correction does not alter the shape of the P-h curve, but only its placement along the horizontal axis.

6.1.6   Apparatus Creep Measurements

As a final correction, the creep of the indenter apparatus may be accounted for in the indentation dwell experiments. To measure the creep of the apparatus, a spherical indentation was performed on silicon while incorporating a 300 s dwell at the peak load. We assume that the spherical indent is mostly elastic so there is very little dislocation motion, and also that the silicon does not creep at room temperature, thus any creep that is observed during the dwell period is attributed to the creep of the indenter apparatus. Figure 6-5 shows the dwell depth versus time curve for a load of approximately 1 N; the observed creep was approximately 0.17 μm after 300 s.
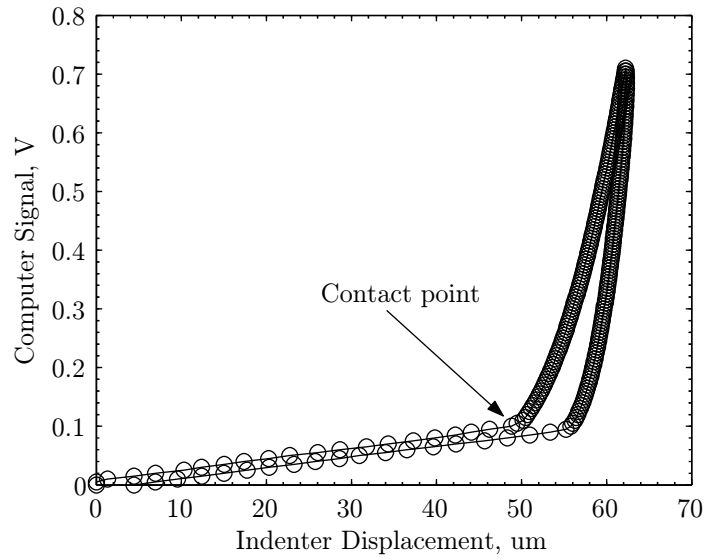
Figure 6-4: Raw data from a microindentation experiment which illustrates the point at which the indenter makes contact with the material. The circles are actual data points, whereas the line simply illustrates the trend.
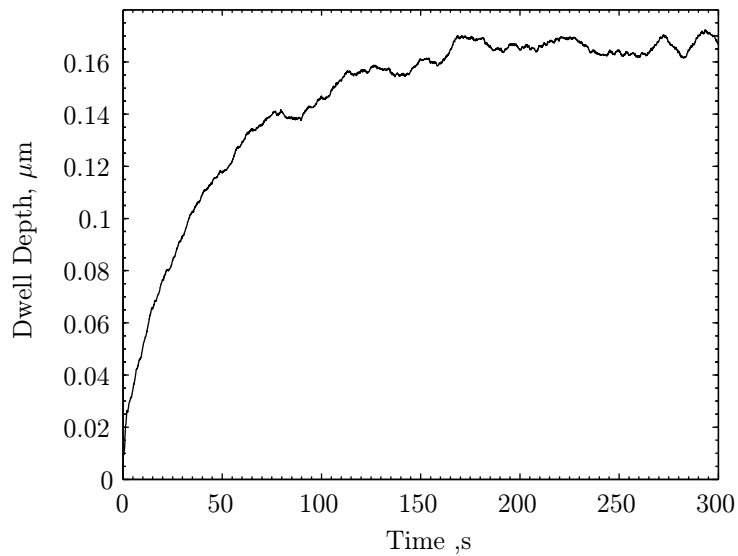

Figure 6-5: Dwell creep results for spherical indentation of silicon at a load of 1N for a dwell time of 300 s. The loading rate prior to the dwell period was 25 mN/s.

6.2 Experimental Results

Figure 6-6 shows force versus depth curves, or P-h curves, for 14 conical indentation experiments on PMMA to a maximum load of approximately 0.64 N at a loading rate of 25 mN/s. The data has been corrected with a compliance factor of 0.7 μm/N. At the peak load, the depth measurements vary from approximately 10.2 μm to 11.0 μm. Figure 6-7 shows the same set of experiments with a zero-offset applied to the data. Essentially, the curves were shifted right on the x-axis until the loading portion of the curves lined up with one another. The shape of the P-h curves are not affected by this shift. As can be seen, the apparent experimental error is reduced considerably once a zero-offset is incorporated. Subsequent experimental results presented here have all been shifted so that the loading portions of all curves are consistent.

Figure 6-8 shows P-h curves for conical indentation experiments to maximum loads of approximately 0.16 N, 0.32 N, and 0.64 N at a loading rate of 25 mN/s. After unloading, approximately 40% of the maximum indentation depth is recovered, which is strongly indicative of the viscoelastic nature of the material. In fact, it has been observed that the material continues to recover even further after the indenter is completely removed from contact, yet this is difficult to measure experimentally with the current apparatus. However, Figure 6-9 shows an experiment where the indenter was held for 300 sec at 10% of the maximum load during unloading. Figure 6-10 shows the recovery depth versus time profile. As can be seen, the material recovers more than 1 μm of depth (or approximately 10% of the maximum depth) in a very short period of time.

One may also notice from the experiments in Figure 6-8 that the curves all exhibit a slight "nose" in the unloading curves, meaning that the indenter depth continues to increase even as the load is decreased. This is commonly observed in creep sensitive materials, and is believed to be due to the fact that the rate of retraction of the indenter cannot keep up with the creep of the material in the opposite direction. This nose in the P-h curves causes problems when one is trying to obtain estimates of the material's elastic properties from the initial unloading slope. Therefore, to eliminate the nose it is common to hold, or "dwell", the indenter at the peak load until the creep rate of the material has slowed, and

then unloading is commenced. Figure 6-11 shows an indentation experiment at a loading rate of 25 mN/s that incorporates a 300 sec dwell time at the maximum load of 0.64 N along with an experiment that incorporates no dwell time. It is apparent that after the dwell, the unloading slope has a substantially different shape than that for the experiment with no dwell time. Dwell experiments for two additional loads of 0.32 N and 0.16 N are shown in Figure 6-12. The amount of creep in the indenter depth with respect to dwell time for each of these experiments is shown in Figure 6-13.

Figure 6-14 shows a P-h curve that was obtained using a Berkovich indenter tip along with a curve obtained for the conical indenter tip. As one can see, there is little difference between the two results.

Figure 6-15 and 6-16 show optical images of a Berkovich indentation into PMMA. The former was taken with a digital camera attached to an optical microscope with polarized lighting. The latter was obtained using a Zygo optical interferometer in order to obtain the height data. The black spots in the 6-16 indicate null data points, so as one can see the maximum depth of indentation has not been resolved. The scale bar may be slightly misleading. What is interesting to note is that the image does show that there is approximately 0.5 μm of pile up in the region where the indenter was once in contact with the material. This pile-up would have had to occur after the indenter was removed from contact, i.e. when the material was undergoing zero-load recovery.
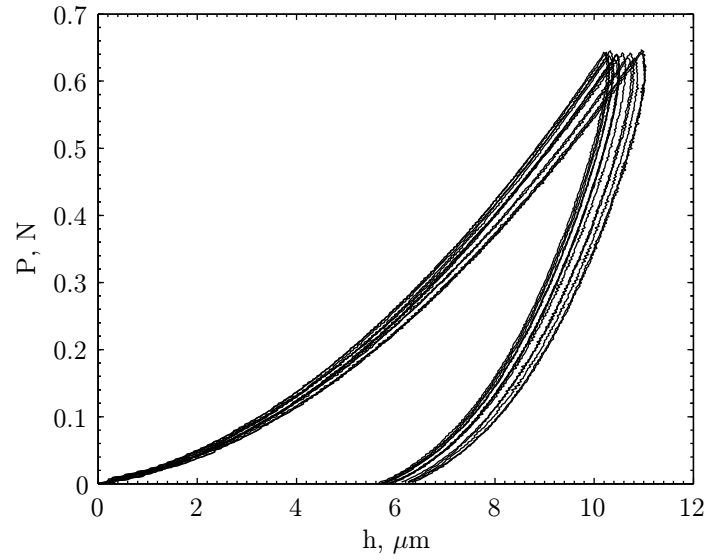
Figure 6-6: Raw compliance-corrected data from 14 microindentation experiments to a maximum load of approximately 0.64 N at a loading rate of 25 mN/s.
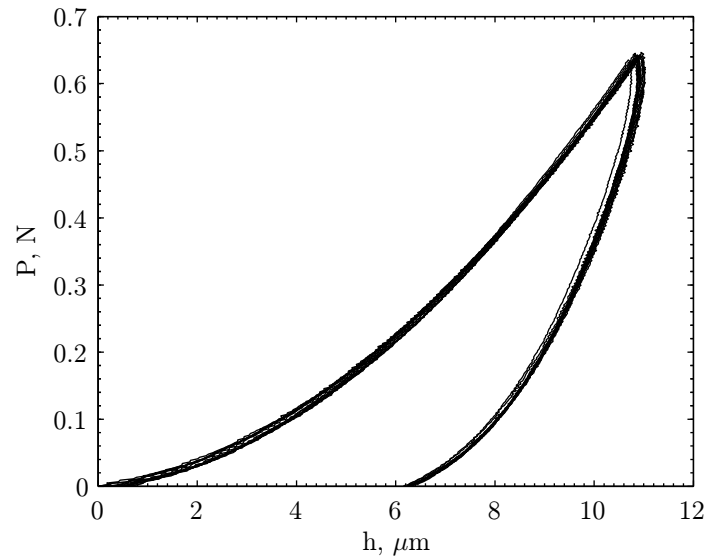

Figure 6-7: Shifted data from 14 microindentation experiments to a maximum load of approximately 0.64 N at a loading rate of 25 mN/s.
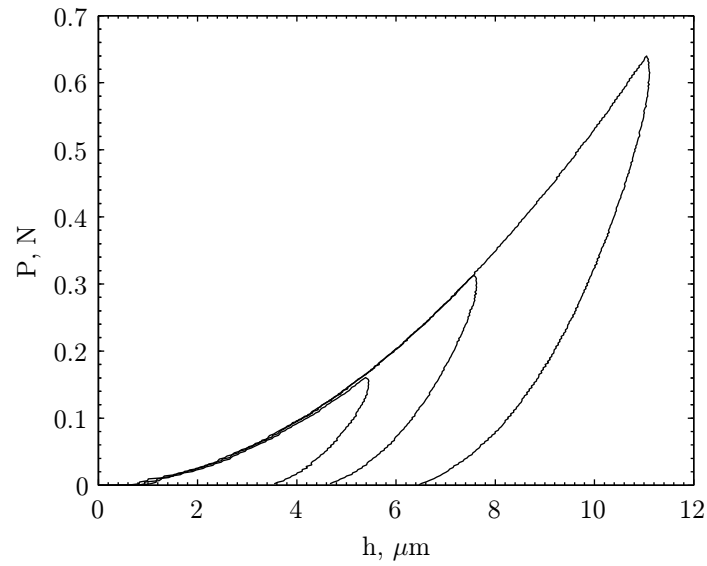
Figure 6-8: Microindentation experiments to maximum loads of 0.64 N, 0.32 N, and 0.16 N at a loading rate of 25 mN/s.
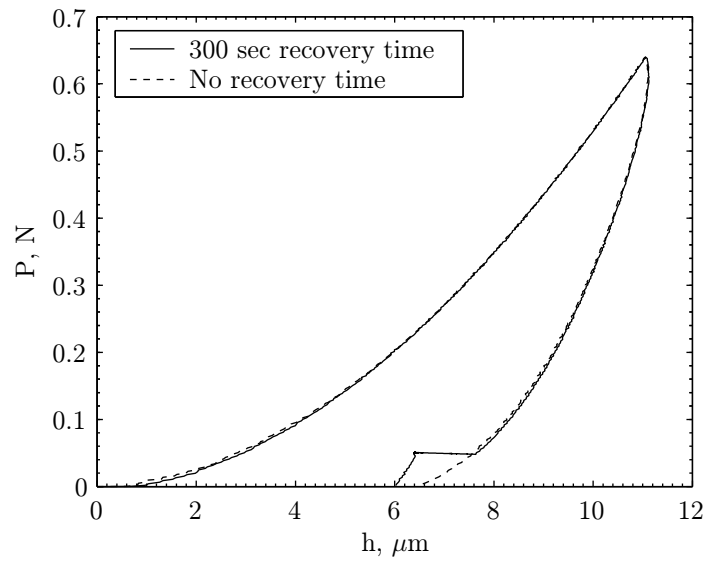
Figure 6-9: Comparison of microindentation experiments incorporating a 300 sec recovery time during unloading at 0.06 N (10% of peak load) and one with no recovery period. The loading rate was 25 mN/s.
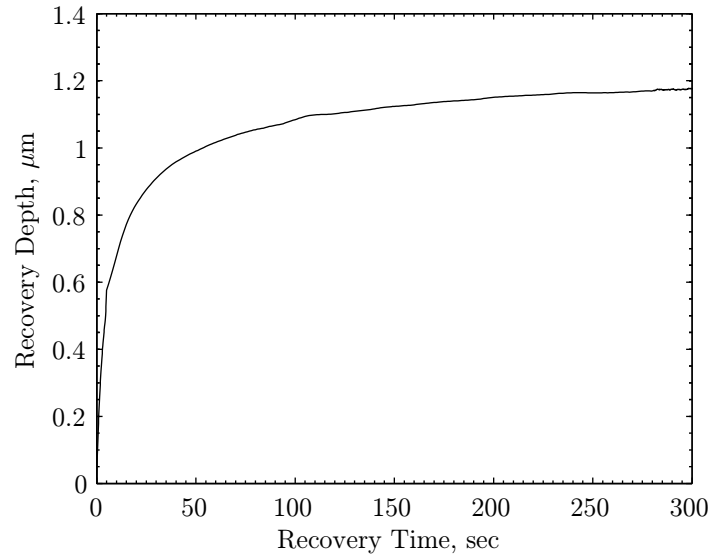
Figure 6-10: Microindentation recovery depth during a 300 sec recovery time during unloading at 0.06 N (10% of peak load) and one with no recovery period. The loading rate prior to the recovery period was 25 mN/s.
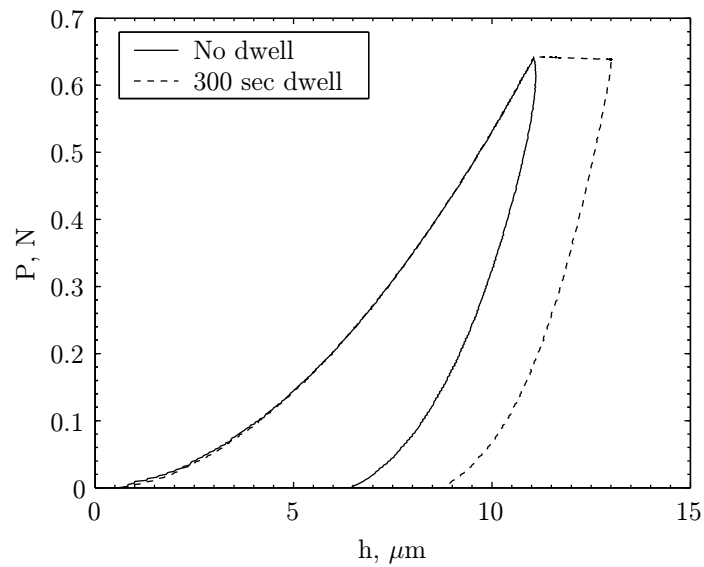
Figure 6-11: Comparison of microindentation experiments with 300 sec dwell time and no dwell time to maximum loads of approximately 0.64 N at a loading rate of 25 mN/s.
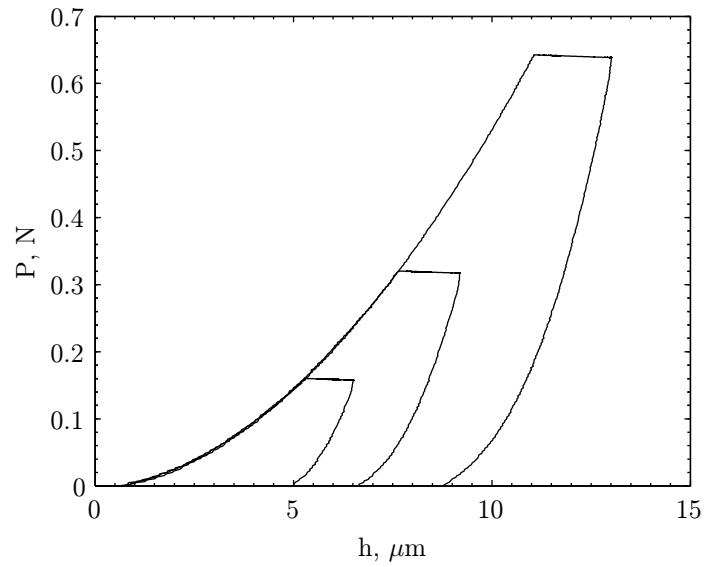
Figure 6-12: Microindentation dwell experiments with a 300 sec dwell time at maximum loads of 0.64 N, 0.32 N and 0.16 N at a loading rate of 25 mN/s.
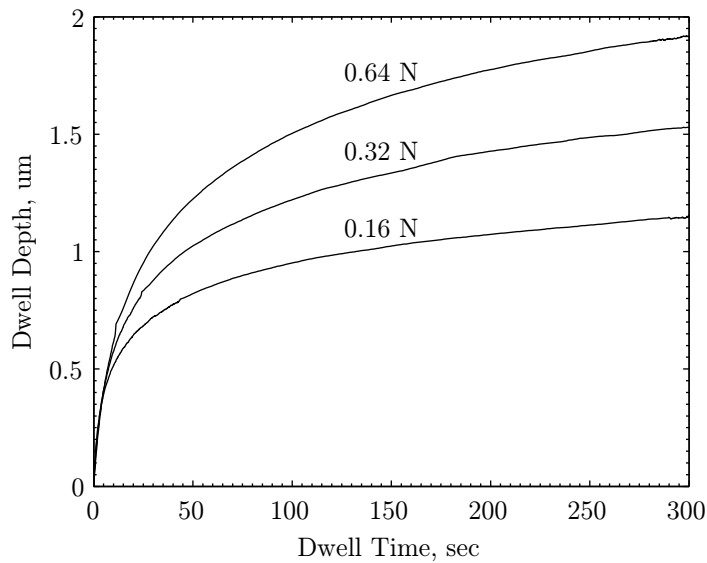
Figure 6-13: Microindentation dwell depths during a 300 sec dwell time at maximum loads of 0.64 N, 0.32 N and 0.16 N. The loading rate prior to the dwell was 25 mN/s.
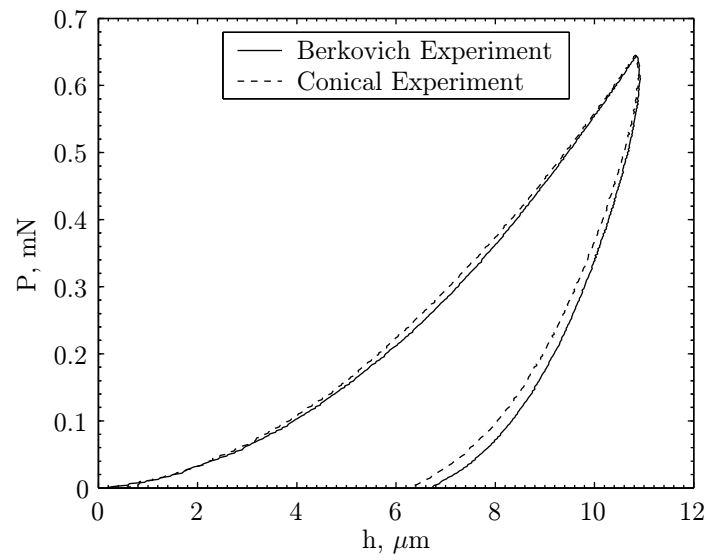
Figure 6-14: Comparison of Berkovich and conical microindentation experiments to max load of 0.64 N.
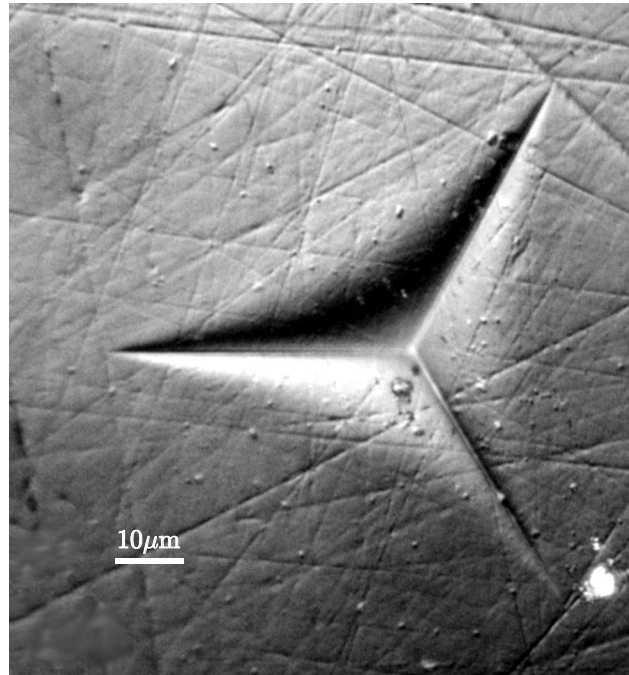
Figure 6-15: Optical image of Berkovich indent to max load of 0.64 N several days after the experiment.
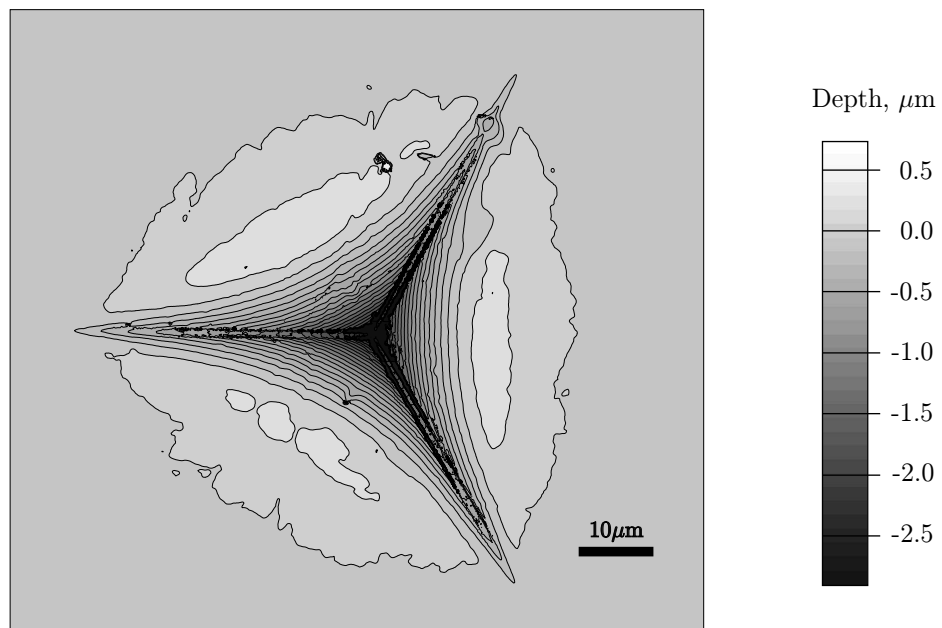
Figure 6-16: Height profile of Berkovich indent to max load of 0.64 N. The Image was obtained using a Zygo optical interferometer several days after the experiment. The black spots indicate null data points. The maximum depth is not resolved in the image.

6.3 Model Verification

In order to verify the model summarized in previous chapters, ABAQUS/Explicit was used to simulate the indentation experiments presented in the previous section. Figure 6-17 shows the axisymmetric mesh used in the conical simulations. The section of PMMA modelled is 200 μm tall and has a radius of 400 μm, which is a sufficient size for the approximately 12 μm indenter penetrations that are expected. The block is meshed with 2940 CAX4R elements and has a higher density near the indenter tip where most of the deformation will be taking place. The mesh density was chosen such that at least 15 elements would contact the indenter at a load of 0.16 N. Figure 6-18 shows the one-sixth symmetry three-dimensional mesh used in the Berkovich simulations. The section of PMMA is of the same dimension as that used for the conical axisymmetric mesh. The block is meshed with 10208 C3D8R elements. In both cases, the indenter is modelled as a rigid surface with a mass of similar order of magnitude as the block of PMMA. One goal of the verification procedure is to check that an axisymmetric conical geometry can substitute for the Berkovich geometry in order to save computation time that would be involved with the 3D calculation.

In both meshes, the indenter is allowed to translate in the 2 direction by means of a given force profile. Figure 6-19 shows the force profile used for the 0.64 N test. Initially, the loading rate is ramped up to the desired rate in order to eliminate numerical problems which occur if the desired rate is applied instantaneously.

Using the parameters for PMMA that were found in Chapter 5, simulations of conical microindentation experiments were conducted at a loading rate of 25 mN/s to loads of approximately 0.16 N, 0.32 N, and 0.64 N. The resulting P-h curves are shown in Figure 6-20 along with the experimental results. The experimental results have been shifted so that the loading portions line up with the simulations. The numerical results are in very good agreement with the experiments. The numerical simulations even exhibit some curvature upon unloading, which was not captured well with the amorphous polymer model used by Gearing (2002). However, the numerical results do not exhibit as strong of a "nose" effect as that which is observed in the experiments.
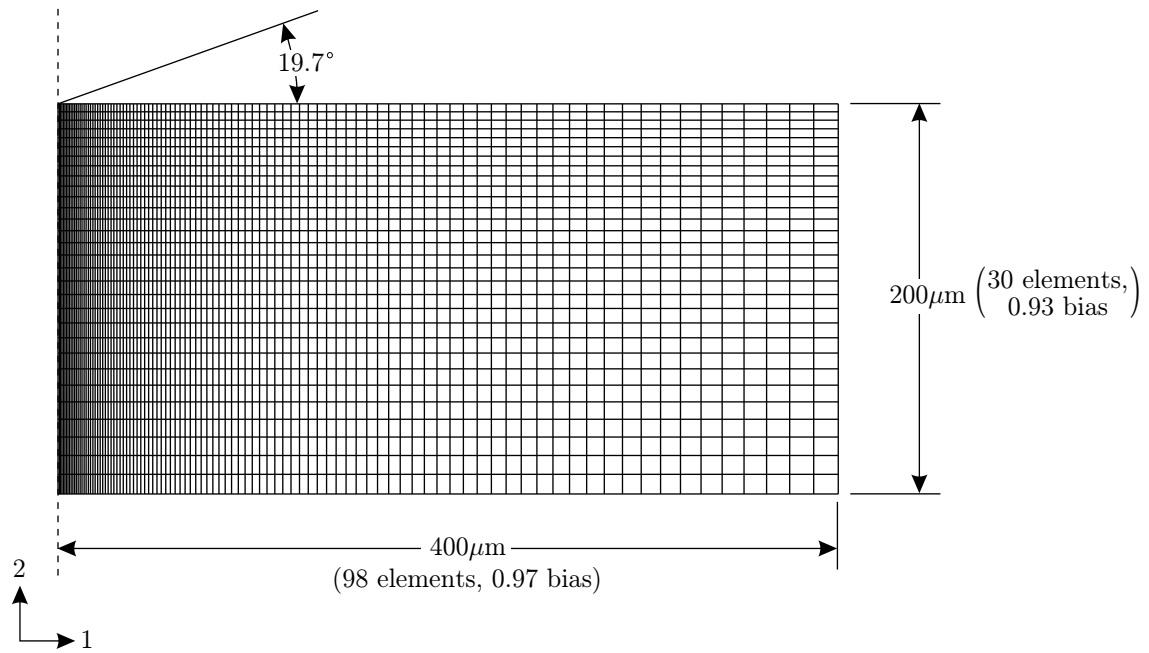
Figure 6-17: Axisymmetric conical indentation mesh used in ABAQUS/Explicit microindentation simulations.
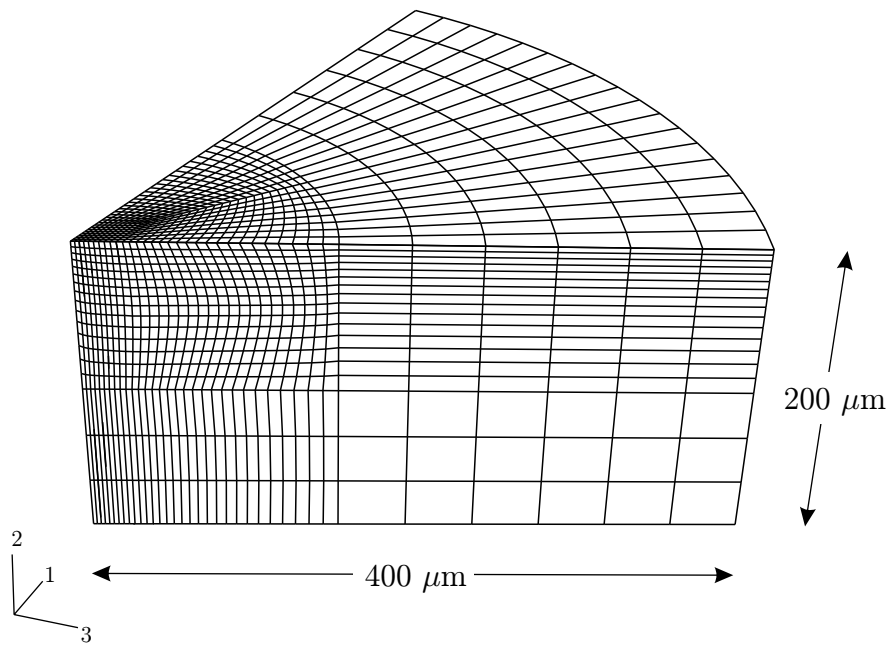

Figure 6-18: One-sixth symmetry Berkovich indentation mesh used in ABAQUS/Explicit microindentation simulations.
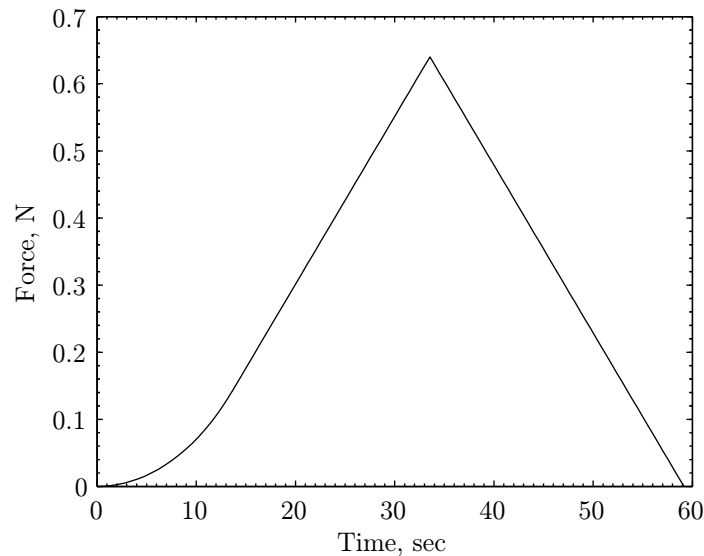
Figure 6-19: Indenter force profile used in microindentation simulations

A simulation of a conical indentation that included a 300 sec dwell time is shown in Figure 6-21 along with the simulation that incorporated no dwell time. There is little change in the initial unloading slopes of the two tests unlike what was observed experimentally.

Dwell simulations and experiments for loads of approximately 0.16 N, 0.32 N, and 0.64 N are shown in Figure 6-22. The corresponding dwell depth versus dwell time curves for the three loads are shown in Figure 6-23. For all loads, the simulations slightly under-predict the dwell depth that is achieved in the experiments, having much better results at lower loads.

A numerical simulation of the indentation recovery experiment is shown in Figure 6-24 along with the recovery depth versus time plots in Figure 6-25. While the numerical results for the dwell experiments performed quite well, the numerical simulation for the recovery experiment does not perform quite as well; it recovers only about 66% of the depth that is observed in the experiment. Furthermore, the simulation shows little change in the unloading slope before and after the recovery period, unlike what is observed in the experiments.

Comparison of the Berkovich experiment and simulation is shown in Figure 6-26. As for the conical experiments and simulations, the simulation matches the experiment quite well. Figure 6-27 shows a comparison of the Berkovich and conical simulations. As in the

experiments, there is little difference in the P-h curves for the two geometries. The strong agreement between the conical and Berkovich simulations verifies the assumption that we may be able to use an axisymmetric conical geometry to represent the Berkovich geometry in order to save computation time.

Figures 6-28 and 6-29 show profiles of Berkovich microindentation after unloading for the simulation and experiment, respectively. The depth contour lines for the simulation show almost no curvature within the indented material region as compared to the experiment. Also, the experiment exhibits some material pileup within the indentation region; in the simulation there is some slight pileup, but it lies outside the indentation region. Clearly, the simulation is not picking up the complex shapes that are formed by the Berkovich indentation experiments. Before further analysis is done, however, it may help to increase the mesh density in the region of the indent.

And finally, figures 6-30 and 6-31 compare the Berkovich microindentation simulation depth contours after unloading and at the peak load, respectively. At the peak load, there is some material sink-in outside the indentation region which appears to recover after unloading.
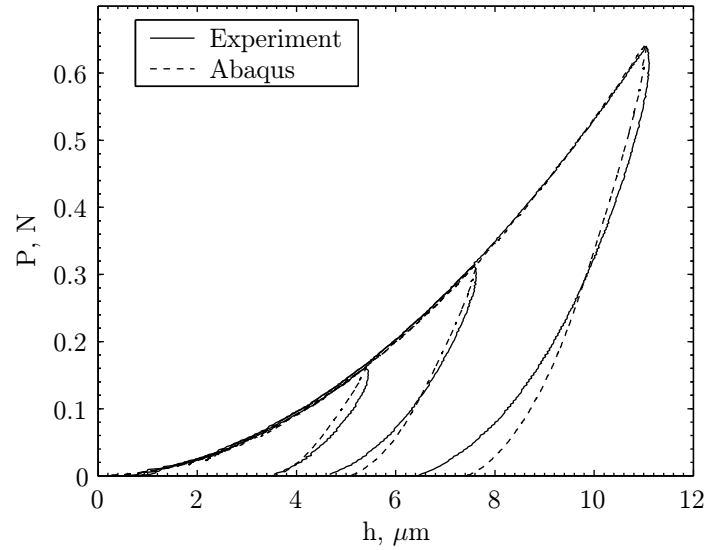
Figure 6-20: Microindentation simulations and experiments to maximum loads of 0.64 N, 0.32 N, and 0.16 N at a loading rate of 25 mN/s.
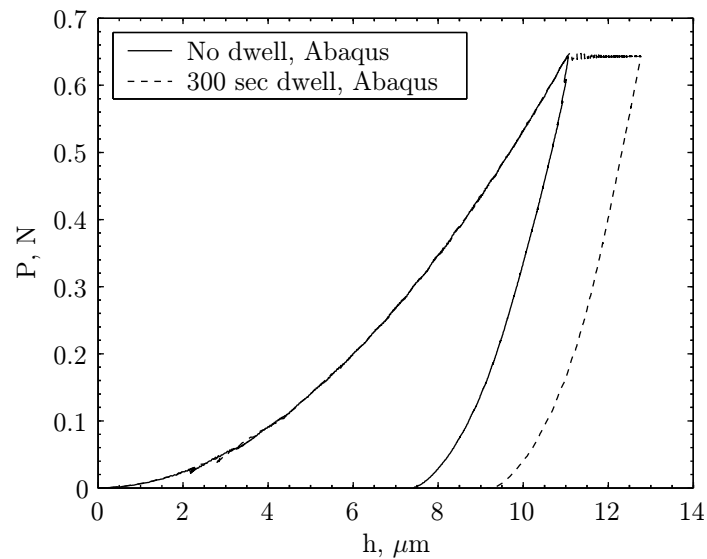
Figure 6-21: Comparison of microindentation simulations with 300 sec dwell time and no dwell time to maximum loads of approximately 0.63 N at a loading rate of 25 mN/s.
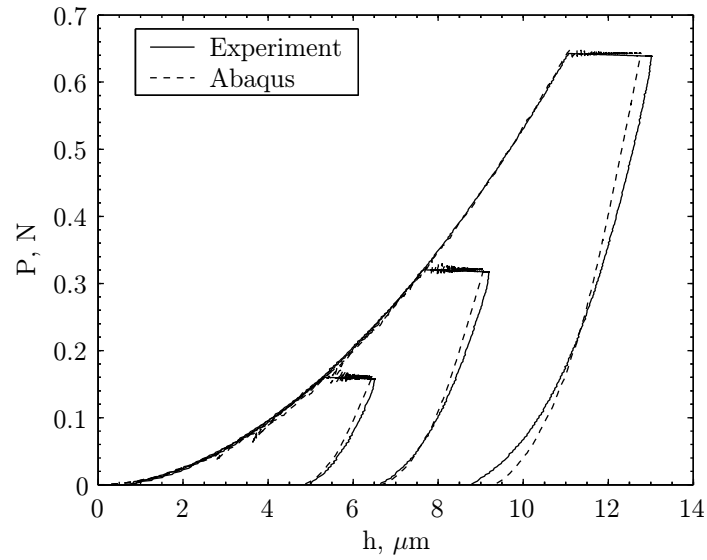
Figure 6-22: Microindentation dwell experiments and simulations with a 300 sec dwell time at maximum loads of 0.64 N, 0.32 N and 0.16 N at a loading rate of 25 mN/s.
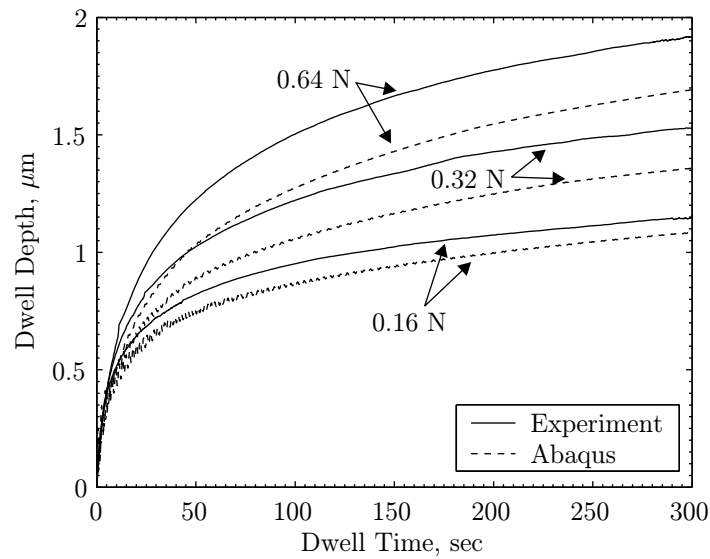
Figure 6-23: Microindentation dwell depths from experiments and simulations during a 300 sec dwell time at maximum loads of 0.64 N, 0.32 N and 0.16 N. The loading rate prior to the dwell was 25 mN/s.
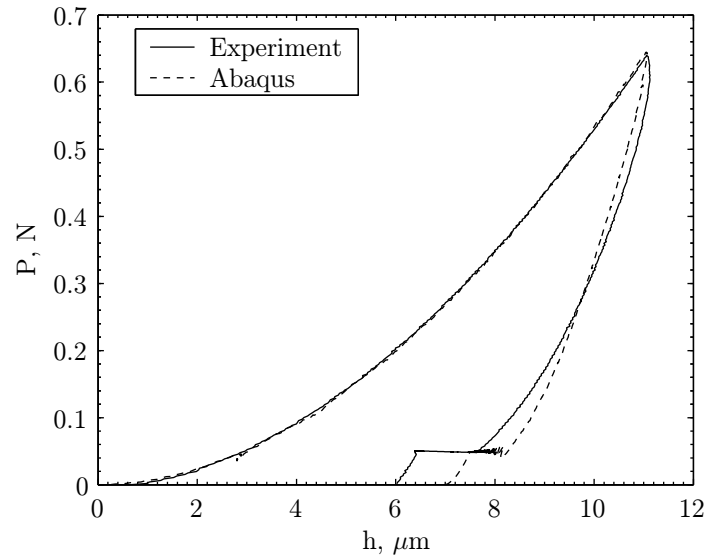
Figure 6-24: Microindentation dwell experiments and simulations with a 300 sec dwell time at maximum loads of 0.64 N, 0.32 N and 0.16 N at a loading rate of 25 mN/s.
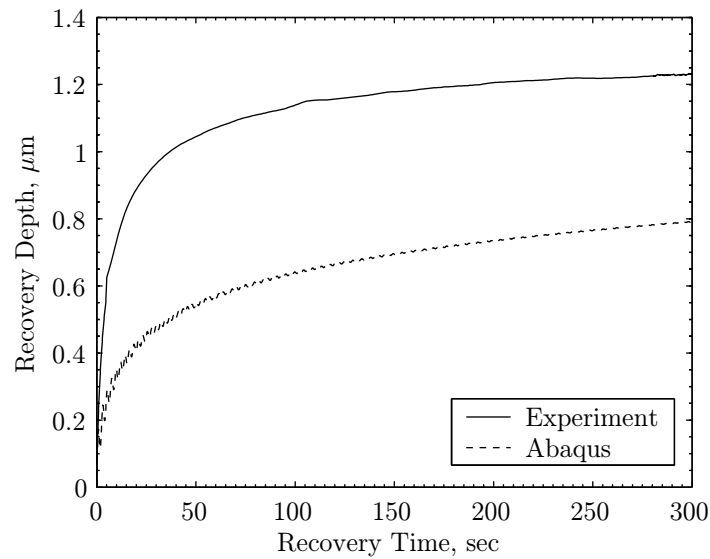
Figure 6-25: Microindentation dwell depths from experiments and simulations during a 300 sec dwell time at maximum loads of 0.64 N, 0.32 N and 0.16 N. The loading rate prior to the dwell was 25 mN/s.
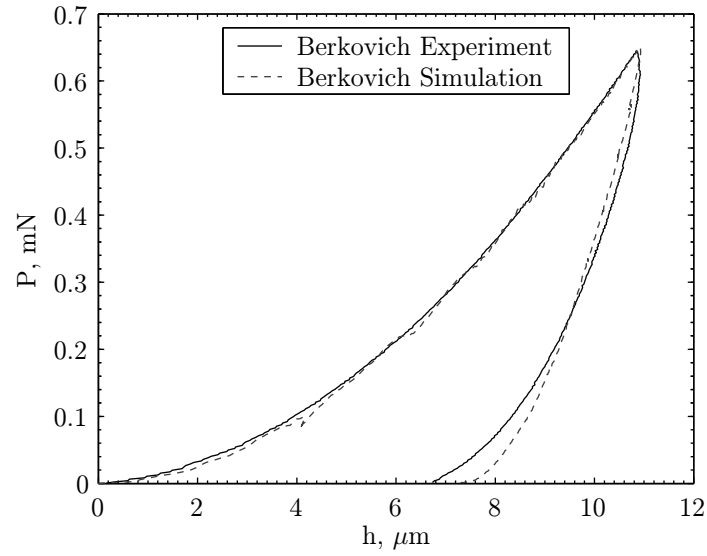
Figure 6-26: Comparison of Berkovich microindentation experiment and simulation.
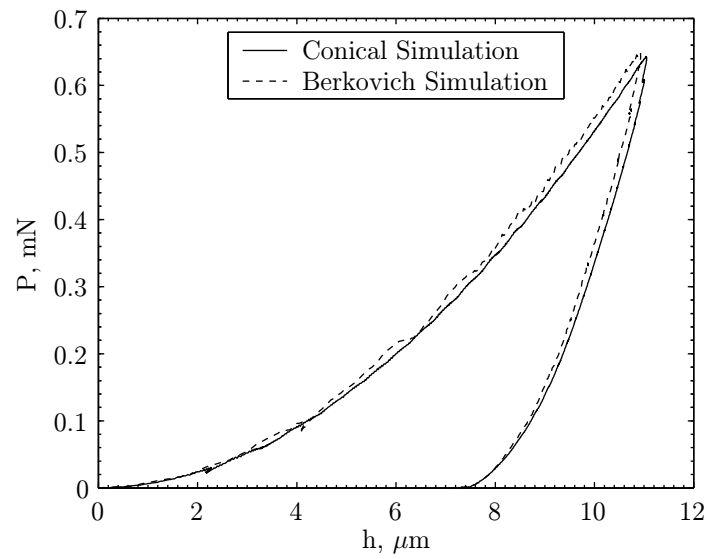
Figure 6-27: Comparison of Berkovich and conical indentation simulations.
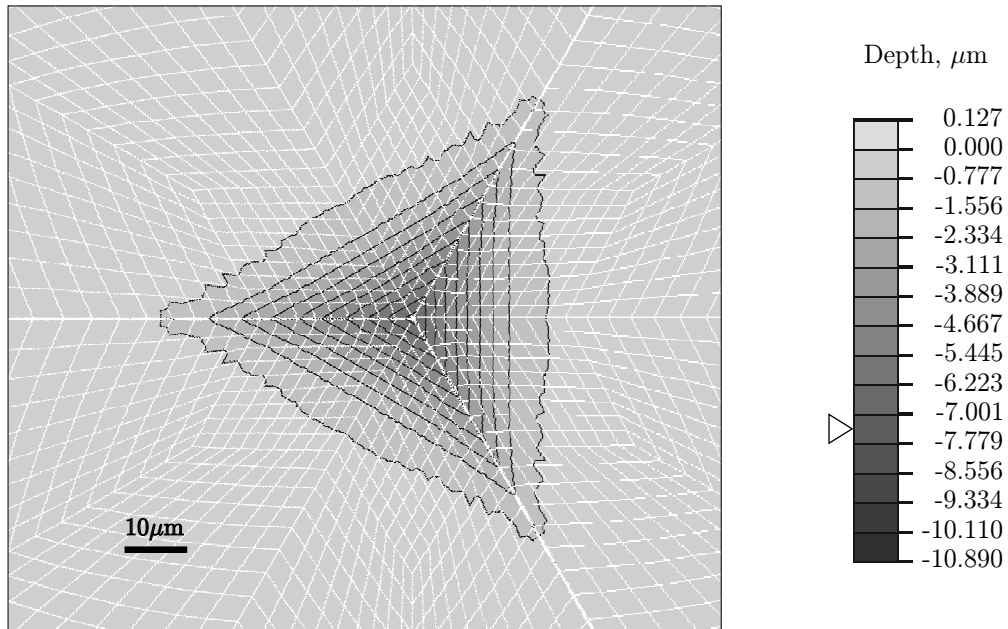
Figure 6-28: Berkovich microindentation simulation surface profile after unloading. The maximum depth in the profile is 7.34 μm. The scale bar was chosen to correspond to the maximum depth at the peak load.
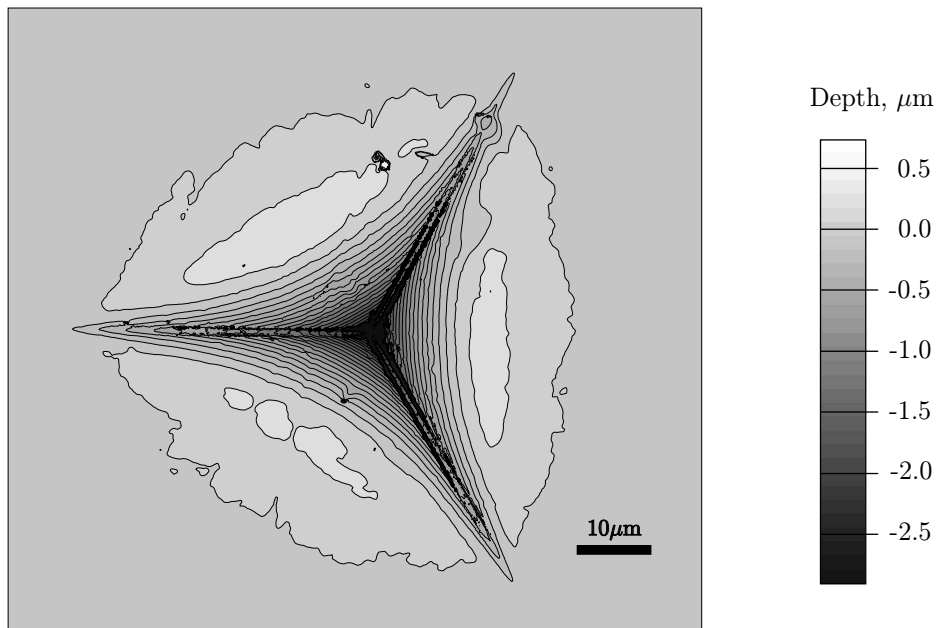
Figure 6-29: Height profile of Berkovich experimental indent to max load of 0.64 N. The Image was obtained using a Zygo optical interferometer several days after the experiment. The black spots indicate null data points. The maximum depth is not resolved in the image.
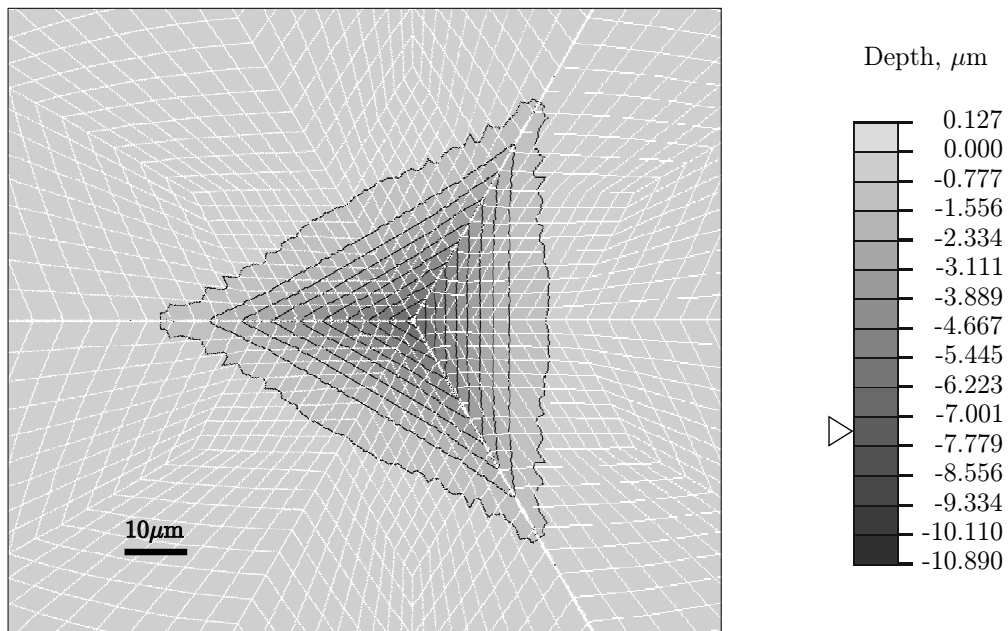
Figure 6-30: Berkovich microindentation simulation surface profile after unloading. The maximum depth in the profile is 7.34 μm. The scale bar was chosen to correspond to the maximum depth at the peak load.
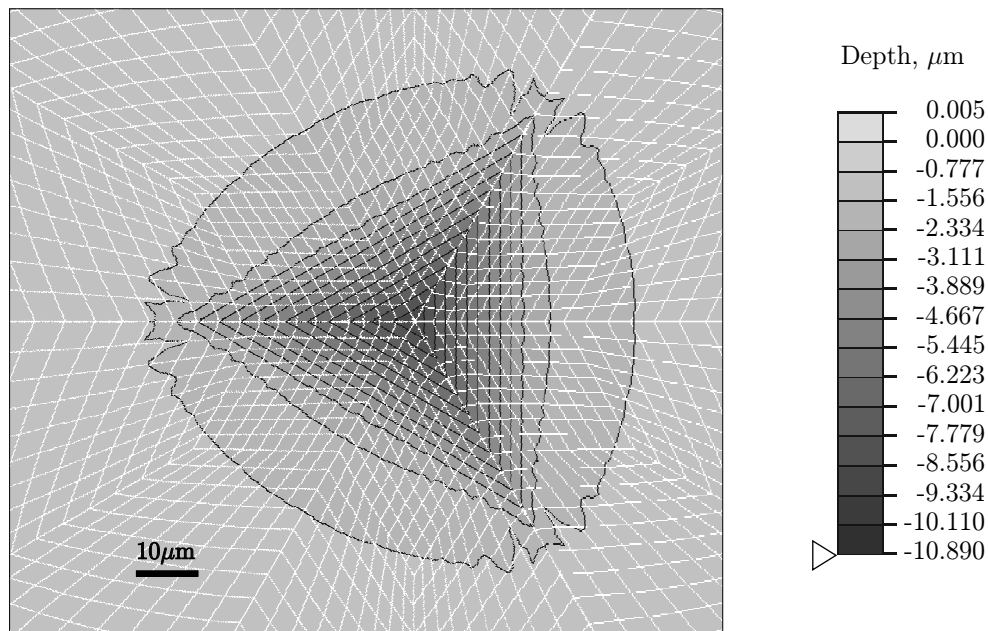
Figure 6-31: Berkovich microindentation simulation surface profile at peak load. The maximum depth in the profile is 10.89 μm

6.4 Discussion

It is clear that the model presented in this work outperforms previous models in its ability to account for the creep response of amorphous glassy polymers at stress levels below those causing "macro-yield", as well as the Bauschinger-type reverse yielding and subsequent zero-load strain recovery phenomena at strain levels less than $\approx 30\%$ associated with the macro-yield transient. While doing so, the model still retains its ability to capture the large strain deformation of this class of materials, all with only one set of material parameters.

As verification, the model predicts the loading shape of conical microindentation experiments very well, and is also able to capture some of the curvature that is observed during the unloading portion of such experiments. Yet, while the model does exhibit the phenomena observed during dwell and recovery periods, there is still some discrepancy between the actual depths achieved during these periods that needs to be resolved. This discrepancy may be due to the fact that the model was calibrated with macro-scale creep and strain recovery experiments at longer time scales (3600 sec and 600 sec respectively versus 300 sec for indentation). Regardless, the results obtained thus far for the microindentation predictions are very promising, and may be very useful in the future for determining material properties of glassy polymers from microindentation tests or for predicting material behavior during micro-scale forging of such materials.

Appendix A

Matlab Code for 1D Model

```
function []=amorphous1D()
% Explicit integration procedure for 1-D amorphous polymer model
%————————————————————-
% all constants are given in 3D values, factor is used
% to convert them to 1D values
factor = sqrt(3);
%
% Read in material properties
%
eyoung      = 3.2d3;                                                    10
mu_r        = 15d0;
lambda_l    = 1.7d0;
s_cv        = 36  * factor;
h_0         = 2.5d3 * (factor^2);
phi_i       = 0;
phi_cv      = 1.0d-3;
g_0         = 0.010;
%
% To increase number of micro-mechanisms, simply increase the size
% of the following vectors, with                                       20
% alpha =    0      1       2       3
s0     = [45      15      25      30   ]*factor;
mu0    = [1       9000    9000    9000 ];
mu_sat = [1       1100    400     200  ];
c      = [0       45d5    18d5    13d5 ];
nu0    = [5d-4    5d-4    5d-4    5d-4 ]/factor;
m      = [.086    .14     .14     .14  ];
% Get number of micro-mechanisms
alpha = length(s0);
%————————————————————-                                                  30
%
% Setup strain profile
```

84

```
%
nreversals = 1;                    % number of reversals
nincr = 5000;                      % increments per reversal

% control  = 'load';
% sigmadot = 10.0;                 %stress rate
% sigmamax = -75;                  %max stress
% sigmamin = 0;                                                    40
% tcreep   = 3600;

control = 'disp';
edot    = 3.d-4;                   % strain rate
emax    = -0.199;                  % max strain
emin    = 0.00;                    % min strain

switch (control)
    case 'load'
        [sigma,t]=creep(sigmamax,sigmadot,tcreep,nincr,nincr);    50
        N = length(sigma);         % maximum number of stress points
        e = zeros(N,1);
    case 'disp'
        [e,t]=cycle(emax,emin,edot,nreversals,nincr);
        N = length(e);             % maximum number of strain points
        sigma = zeros(N,1);
end
%————————————————-
% Initialization
%                                                                 60
Up       = zeros(N,1);
Up(1)    = 1;
phi      = zeros(N,1);
s        = zeros(N,alpha);
s(1,:)   = s0;
mu       = zeros(N,alpha);
mu(1,:)  = mu0;
A        = zeros(N,alpha);
A(1,:)   = 1;
%                                                                 70
sigmaeff = zeros(1,alpha);
nup      = zeros(1,alpha);
Dp       = zeros(1,alpha);
Tback    = zeros(1,alpha);
T_A      = 0;
T_B      = 0;
%
```

```matlab
%——————————————————-
%
%  Begin Computation                                              80
%
for n=1:N−1
    delt = t(n+1) − t(n);
%
% Calculate the stress due to B system
%
    U = exp(e(n));
    Ubar = sqrt(U*U + 2/U)/sqrt(3);
    arg = Ubar / lambda_l;
    if ( 0 < abs(arg)  < 0.84136d0)                               90
        invlang = 1.31446d0 * tan(1.58986d0*arg) + 0.91209d0*arg;
    elseif (   abs(arg)  < 1.0 )
        invlang = 1.d0/(sign(arg) − arg);
    else
        'error in inverse langevin argument'
    end
    mu_lang = mu_r * lambda_l / (3.d0 * Ubar) * invlang; % Back stress modulus
    T_B     = mu_lang * (U*U − 1/U);
%
% Calculate the plastic stretching due to the A system           100
%
    Tback    = mu(n,:) .* (A(n,:).*A(n,:) − 1./A(n,:));
    sigmaeff = T_A − Tback;
    nup      = nu0.*(abs(sigmaeff)./s(n,:)).^(1./m);
    Dp       = nup .* sign(sigmaeff);
%
%————————————————
%
% Update Up
%                                                                 110
    Up(n+1) = Up(n) + delt * sum(Dp) * Up(n);
%
% Update the free volume
%
    if (phi(n) <=  phi_cv)
        phi_dot = g_0*((s(n,1)/s_cv) − 1)*nup(1);
    else
        phi_dot = 0;
    end
    phi(n+1) = phi(n) + phi_dot *delt;                            120
%
% Update the mu's
```

```
%
    mu_dot = c .* (1 − (mu(n,:)./mu_sat)) * phi_dot;
    mu(n+1,:) = mu(n,:) + mu_dot * delt;
%
% Update the s's
%
    s_sat     = s_cv *( 1. + b*(phi_cv − phi(n)));
    arg       = 1 − s(n,1)/s_sat;                                        130
    s_dot     = h_0 * arg  * nup(1);
    s(n+1,1) = s(n,1) + s_dot*delt;
    s(n+1,2:alpha) = s(n,2:alpha);
%
% Update the A coeffs.
%
    A(n+1,:) = A(n,:) + (Dp.*A(n,:))*delt;
%
%—————————————————————
%                                                                       140
% Update stress/strain
%
    switch (control)
        case 'load'
            T_A       = sigma(n+1) − T_B;
            Ee        = T_A/eyoung;
            Ue        = Ee + 1;
            U         = Ue*Up(n+1);
            e(n+1)    = log(U);
        case 'disp'                                                      150
            U            = exp(e(n+1));
            Ue           = U/Up(n+1);
            Ee           = Ue − 1;
            T_A          = eyoung * Ee;
            sigma(n+1) = T_A + T_B;
    end
end
%%%%%%%%%%%%%%%%%%%%%%%%%%%%%%%%%%%%%%%%%%%%%%%%%

function [x,t] = cycle(xmax,xmin,xdot,numrev,Nstep)
% CYCLE    Returns vectors of x and time for cyclic x.
%    [x,t] = CYCLE(xmax,xmin,xdot,numrev,Nstep) returns vectors of x and time for
%    cyclic x, where:
%    x is the returned x vector
%    t is the returned time vector
%    xmax is the maximum x
%    xmin is the minimum x
```

```matlab
%      xdot is the x rate (sign ignored)
%      numrev is the number of cycles, rev 0 from 0 to xmax,              10
%                                    rev 1 from xmax to xmin,
%                                    rev 2 from xmin to xmax, etc.
%      Nstep is the number of increments per cycle step (0 inclusive)

if nargin ~= 5
   error('Not enough input arguments.');
end
if xmax == xmin
    error('xmax must not be equal to xmin');
end                                                                       20
if numrev < 0
    error('numrev must be greater than or equal to 0');
end
if Nstep < 2
    error('Nstep must be greater than or equal to 2');
end
numrev=floor(numrev);
Nstep=floor(Nstep);
N = Nstep * (numrev+1);
t=zeros(N,1);                                                             30
x=zeros(N,1);

t1 = abs(xmax/xdot);
t2 = abs((xmax−xmin)/xdot);
delt1 = t1/Nstep;
delx1 = xmax/Nstep;
delt2 = t2/Nstep;
delx2 = (xmax−xmin)/Nstep;
n=2;
                                                                          40
for i=1:Nstep
    x(n) = x(n−1) + delx1;
    t(n) = t(n−1) + delt1;
    n=n+1;
end


for i=1:numrev;
    delx2 = −delx2; %alternates between loading and unloading
    for i=1:Nstep
        x(n) = x(n−1) + delx2;                                           50
        t(n) = t(n−1) + delt2;
        n=n+1;
    end
```

```matlab
end
%%%%%%%%%%%%%%%%%%%%%%%%%%%%%%%%%%%%%%%%%%%

function [x,t] = creep(xmax,xdot,tcreep,Nstep,Ncreep)
% CREEP   Returns vectors of x and time for given creep history.
%    [x,t] = CREEP(xmax,xdot,tcreep,Nstep,Ncreep) returns vectors of x and time
%     for given creep histroy, where:
%    x is the returned x vector
%    t is the returned time vector
%    xmax is the vector of max change of x value before creeping
%    xdot is the vector of the x rates (sign ignored)
%    tcreep is the vector of creep times
%    Nstep is the number of increments while not creeping (vector or scalar)
%    Ncreep is the number of increments while creeping (vector or scalar)

if nargin ~= 5
   error('Not enough input arguments.');
end

numcreeps = length(xmax);
Nstep=floor(Nstep);
Ncreep=floor(Ncreep);
N = sum(Nstep)+sum(Ncreep);
t=zeros(N,1);
x=zeros(N,1);

delt_creep = tcreep./Ncreep;
n=2;

for i=1:numcreeps
    for j=1:Nstep(i)
        if i == 1
            x0=0;
        else
            x0=xmax(i-1);
        end
        tstep = abs((xmax(i) - x0))/xdot(i);
        delt(i) = tstep/Nstep(i);
        delx(i) = (xmax(i) - x0)/Nstep(i);
        x(n) = x(n-1) + delx(i);
        t(n) = t(n-1) + delt(i);
        n=n+1;
    end
    for j=1:Ncreep(i)
        x(n) = x(n-1);
```

```
        t(n) = t(n-1) + delt_creep(i);
        n=n+1;
    end
end
```

References

ABAQUS, Inc. (2002). *ABAQUS Reference Manuals.* Pawtucket, RI.

Anand, L. (2003). A finite deformation internal variable model for the visco-elastic-plastic response of amorphous polymers. In preparation.

Anand, L., & Gurtin, M. E. (2003). A theory of amorphous solids undergoing large deformations, with application to polymeric glasses. *InternationalJournal of Solids and Structures, 40*(6), 1465-1487.

Arruda, E. M., & Boyce, M. C. (1993). Evolution of plastic anisotropy in amorphous polymers during finite straining. *International Journal of Plasticity, 9*, 697-720.

BEI, Kimco Magnetics Division. (1994). *Drawing for Linear Actuator LA13-12-000(LTR).* San Marcos, CA.

Boyce, M. C., Parks, D. M., & Argon, A. S. (1998). Large inelastic deformation of glassy polymers. part 1: Rate-dependent constitutive model. *Mechanics of Materials, 7*, 15-33.

Briscoe, B. J., Fiori, L., & Pelillo, E. (1998). Nano-indentation of polymeric surfaces. *Journal of Physics, D: Applied Physics, 31*, 2395-2405.

Briscoe, B. J., & Sebastian, K. S. (1996). The elastoplastic response of poly(methyl methacrylate) to indentation. *Proceedings of the Royal Society of London, A, 452*, 439-457.

Briscoe, B. J., Sebastian, K. S., & Adams, M. J. (1994). The effect of indenter geometry on the elastic response to indentation. *Journal of Physics, D, 27*, 1156-1162.

Cheng, Y. T., & Cheng, C. M. (1998). Scaling approach to conical indentation of elastic-plastic solids with work-hardening. *Journal of Applied Physics, 84*, 1284-1291.

Cheng, Y. T., & Cheng, C. M. (1999). Scaling relationships in conical indentation of elastic-perfectly plastic solids. *International Journal of Solids and Structures, 36*, 1231-1243.

Doerner, M. F., & Nix, W. D. (1986). A method for interpreting the data from depth-sensing indentation instruments. *Journal of Materials Research, 1*(4), 601-609.

Fischer-Cripps, A. C. (2002). *Nanoindentation.* New York: Springer-Verlag.

Gearing, B. P. (2002). *Constitutive equations and failure criteria for amorphous polymeric solids.* Unpublished doctoral dissertation, Massachusetts Institute of Technology.

Hasan, O. A. (1994). *An experimental and analytical investigation of the thermomechanical properties of glassy polymers.* Unpublished doctoral dissertation, Massachusetts Institute of Technology.

Ion, R. H., Pollock, H. M., & Roques-Carmes, C. (1990). Micron-scale indentation of amorphous and drawn PET surfaces. *Journal of Materials Science, 25*(2B), 14444-1454.

Kroner, E. (1960). Allgemeine kontinuumstheorie der versetzungen und eigenspannungen. *Archive for Rational Mechanics and Analysis, 4,* 273-334.

Lee, E. H. (1969). Elastic plastic deformation at finite strain. *ASME Journal of Applied Mechanics, 36,* 1-6.

Oliver, W. C., & Pharr, G. M. (1992). An improved technique for determining hardness and elastic modulus using load and displacement sensing indentation experiments. *Journal of Materials Research, 7*(6), 1564-1583.

Parks, D. M., Argon, A. S., & Bagepalli, B. (1985). *Large elastic-plastic deformation of glassy polymers, part 1: Constitutive modelling* (Tech. Rep.). MIT, Program in Polymer Science and Technology Report.

Van Landingham, M. R., Villarrubia, J. S., Guthrie, W. F., & Meyers, G. F. (2001). Nanoindentation of polymers: an overview. In V. V. Tsukruk & N. D. Spencer (Eds.), *Recent Advances in Scanning Probe Microscopy, Proceedings of the 220th American Chemical Society National Meeting, August 2000* (p. 15-43). Washington D. C.: Wiley-VCH Verlag GmbH.

van Melick, H. G. H., Bressers, O. F. J. T., den Toonder, J. M. J., Govaert, L. E., & Meijer, H. E. H. (2003). A micro-indentation method for probing the craze-initiation stress in glassy polymers. *Polymer, 44,* 2481-2491.

Wu, P. D., & Van der Giessen, E. (1993). On improved network models for rubber elasticity and their applications to orientation hardening of glassy polymers. *Journal of the Mechanics and Physics of Solids, 41,* 427-456.